

High-Performance Quantum Cascade Lasers Grown by Metal-Organic Vapor Phase Epitaxy and Their Applications to Trace Gas Sensing

Mariano Troccoli, *Member, IEEE, Member, OSA*, Laurent Diehl, David P. Bour, *Fellow, IEEE*, Scott W. Corzine, Nanfang Yu, Christine Y. Wang, Mikhail A. Belkin, Gloria Höfler, Rafal Lewicki, Gerard Wysocki, Frank K. Tittel, *Fellow, IEEE*, and Federico Capasso, *Fellow, IEEE, Fellow, OSA*

(Invited Paper)

Abstract—We present an overview of our results on the design, material growth, device characterization, and spectroscopic applications of MOVPE-grown quantum cascade lasers (QCLs). These devices are capable of room-temperature (RT) continuous-wave operation and high power emission. The first section focuses on growth of laser material, device fabrication, and quantum design. The second section discusses RT pulsed operation, in particular the doping dependence of laser performance and broadband emission. Near-field measurements performed on the devices' facets correlating lateral modes to device size are also discussed. Section III deals with continuous-wave high-temperature operation from lasers with different active region designs, including their spectral characteristics and in the emergence of coherent phenomena at high power levels. Section IV analyses the devices thermal dissipation capabilities, while in Section V we report reliability data. The final section focuses on spectroscopic applications and tunability. Optofluidic narrow ridge lasers and their application to chemical sensing are reported along with recent data on a broadband on chip spectrometer consisting of individually addressable distributed feedback QCLs. Various spectroscopic techniques and in particular quartz-enhanced photoacoustic absorption spectroscopy and its use in gas sensing systems are discussed. Finally, optofluidic narrow ridge lasers and their applications to fluid sensing are presented.

Index Terms—Infrared spectroscopy, semiconductor device fabrication, semiconductor lasers.

Manuscript received October 11, 2007; revised February 22, 2008. Current version published January 28, 2009. This work was supported by Agilent Technologies, by the Air Force Office of Scientific Research (AFOSR MURI on Plasmonics), by the DARPA Optofluidics Center under Grant HR0011-04-1-0032, by the U.S. Army Research Laboratory and the U.S. Army Research Office under Grant W911NF-04-1-0253, and by the Center for Nanoscale Systems (CNS) at Harvard University. Harvard-CNS is a member of the National Nanotechnology Infrastructure Network (NNIN).

M. Troccoli was with Harvard University, Cambridge, MA 02138 USA. He is now with Argos Tech LLC, Santa Clara, CA 95051 USA (e-mail: mtroccoli@argostechinc.com).

L. Diehl, N. Yu, C. Y. Wang, M. A. Belkin, and F. Capasso are with the School of Engineering and Applied Sciences, Harvard University, Cambridge, MA 02138 USA (e-mail: capasso@seas.harvard.edu).

D. P. Bour was with Agilent Labs, Palo Alto, CA 94304 USA. He is now with Photodigm, Inc., Richardson, TX 75081 USA.

S. W. Corzine was with Agilent Labs, Palo Alto, CA 94304 USA. He is now with Infinera HQ, Sunnyvale, CA 94089 USA.

G. Höfler was with Agilent Labs, Palo Alto, CA 94304 USA. She is now with Argos Tech LLC, Santa Clara, CA 95051 USA.

R. Lewicki, G. Wysocki and F. K. Tittel are with the Electrical and Computer Engineering Department, Rice University, Houston, TX 77005 USA.

Color versions of one or more of the figures in this paper are available online at <http://ieeexplore.ieee.org>.

Digital Object Identifier 10.1109/JLT.2008.925056

I. INTRODUCTION

QUANTUM CASCADE (QC) lasers have experienced a constant development since their invention at Bell Labs in 1994 [1] and represent so far the most interesting new source for optical systems operating in the mid-infrared (mid-IR), i.e. $\lambda = 3\text{--}25\ \mu\text{m}$, and in the THz region of the spectrum ($\lambda = 50\text{--}180\ \mu\text{m}$) [2], [3]. Innovation in device engineering of QC lasers has been supported all along by an equally intensive material development effort. The operating principle of QC lasers has in fact been demonstrated in different material systems [4]–[6] and with various growth techniques [7]–[9], overall proving QC lasers to be a robust technology platform for the mid-infrared.

The QC laser material structure poses several challenges to the growth process: the total thickness can easily reach ten microns, the number of interfaces is typically in the hundreds, the smallest layer thickness can be as little as few monolayers, and the laser performance is sensitive to background doping and interface roughness. Having a consistently reproducible high-quality source of material for QC lasers is therefore one of the key elements to its manufacturability.

The main characteristic that sets QC lasers apart from common diode lasers is that they are unipolar devices, i.e. they employ only one type of carrier/doping. QCL operation relies on transitions between electronic states created by quantum confinement within the conduction band of the laser materials (intra-band), as opposed to the inter-band transitions taking place in p-n junction diode lasers. Band structure engineering in QC devices allows significant control over important laser characteristics such as its wavelength, threshold, optical power, and even its high-temperature performance.

Band structure engineering makes it possible to tailor the laser design so that its optical emission characteristics can be targeted to specific purposes. QC lasers design innovations so far have included: short-wavelength [5], [10] or long-wavelength [11] emission, high power output [12], nonlinear optical generation [13]–[15] vertical emission [16], and Terahertz generation [17], among others.

The resulting complexity of the active region structure has been in most cases a drawback for the optimization of the laser thermal performances. A typical QC laser has a 1- to

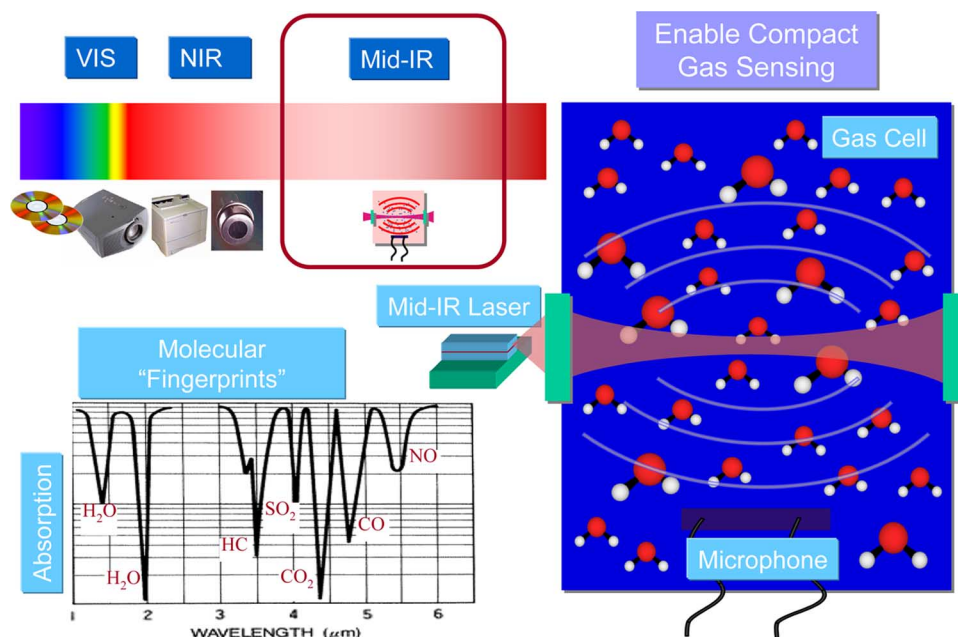


Fig. 1. Compact tunable source can enable high-sensitivity portable photoacoustic sensors for gas analysis in the molecular fingerprint region (the mid-IR region of the electromagnetic spectrum). Several important compounds have their signature absorption resonances in this region.

2- μm -thick active region including hundreds of interfaces, whose typical thermal conductivity is therefore low (about 10 K/W) [18]. In addition, the active region transport is controlled by intersubband transitions with intrinsically short lifetimes (sub-picosecond) and typically requires a bias of several volts at threshold for laser action. This results in high threshold current densities (1 kA/cm² or more) and a large amount of heat to be dissipated ($\sim 5\text{--}10$ W) in a device with low thermal conductivity, thus pushing the QC active region temperature several tens of degrees (30–80 K) above the heat sink one.

As a consequence, while room-temperature (RT) pulsed operation was achieved soon after the first laser demonstration, continuous-wave (CW) RT operation has been elusive for quite a while. Room temperature CW operation was first demonstrated in a laser grown by MBE [19] but more recently we were able to demonstrate CW RT operation in an MOVPE-grown QC laser, both for lattice matched and for strained material systems [20]–[24]. This is a key step towards the industrial implementation and production of QC technology.

CW RT operation of QC lasers with high reliability and low power consumption will enable compact and versatile optical sensors (see Fig. 1 for a schematic illustration of optical gas analysis). In the case of the more mature p-n diode lasers ($\lambda < 3\ \mu\text{m}$), compactness and reliability have been the key to high-volume low-cost applications of optical technology in data storage, imaging, and telecommunications. Analogously, the emergence of volume applications for QCL-based systems will depend on the efficiency and reliability of the optical sources, thus allowing the deployment of small and portable sensing systems.

Presently, interesting applications employing mid-IR sources are in the fields of industrial process monitoring, noninvasive diagnostics, security and defense, free space communications, among others. Most of these are based on some type of spectroscopic analysis (chemical process monitoring, hazardous substance detection, biomedical diagnostics) but a significant frac-

tion of present applications is also concerned with high-power laser operation over long distances (IR countermeasures, free-space optics, remote sensing). In all these fields, QCLs can have an impact because of their portability, wavelength agility, robustness, and power.

II. MATERIAL GROWTH AND CHARACTERIZATION

For growth of high-performance QCL heterostructures, several requirements must be fulfilled. Foremost among these is the ability to form atomically abrupt interfaces between layers of nanometer or even sub-nm thickness. Molecular beam epitaxy (MBE) is exemplary in this regard, however a properly designed MOCVD reactor can approach the interface abruptness associated with MBE. Low background doping, in concert with controlled intentional-doping profiles, are also critical for QC lasers in order to minimize the gain spectrum width and to reduce thresholds. This requirement may represent a limitation for AlGaAs-based QCLs by MOCVD, since carbon contamination is always present in MOCVD-grown AlGaAs. However, carbon contamination is generally not present in the AlInAs and GaInAs alloys grown by MOCVD. Therefore these InP-based alloys are a natural choice for MOCVD-grown QCLs. In addition, MOCVD may even offer some advantages over MBE for QCL growth.

Among the anticipated benefits of MOCVD are stability of growth rate and composition over very long runs, the ease of achieving low oxygen contamination in aluminum-containing materials, the ability to grow thick InP cladding- and burying-layers, and the potential for very fast growth rates. On the other hand, it is expected that interface formation is more challenging for MOCVD; and also the requirement for organic precursors might lead to unacceptably high carbon background for some materials.

We have grown AlInAs/GaInAs quantum cascade laser (QCL) structures by conventional, low-pressure (76 Torr)

MOVPE. Growth was performed at Agilent Labs facilities. Both lattice matched (to the InP substrate) and strain balanced structures were prepared, similar to those described in [25], [26]. Our reactor incorporates a purged and pressure-balanced switching manifold and a close-spaced showerhead injector. Similar to the conditions employed in [7], the optimum growth rate for the quantum cascade active region was set very low (0.1 nm/s). The remainder of the structure was grown at approximately 5 times this rate. Precursors include trimethylindium, triethylgallium (for the slow-grown QC structure only), trimethylgallium, trimethylaluminum, arsine, and phosphine. Since the n-type doping profile in the injector region is critical for QCL operation, silicon was chosen as the n-type dopant, from the precursor disilane (0.01% in H₂). Disilane exhibits excellent transient characteristics during MOCVD growth, in contrast to the group-VI donors, whose precursors tend to suffer from a turn-on-delay and memory effect in the reactor. The samples were grown on (001)-oriented InP:S ($n = 3 \times 10^{18} \text{ cm}^{-3}$) substrates.

The choice of growth temperature represents a tradeoff between the need for low oxygen contamination and smooth surfaces during growth, favored by high growth temperature, and the need for low background shallow impurity concentration and preservation of the interface quality, improved at lower temperatures.

To avoid excessive free-carrier loss associated with the high doping in the substrate, a relatively thick ($3 \mu\text{m}$) low-doped n-type InP:Si ($n = 1 \times 10^{17} \text{ cm}^{-3}$) cladding layer was grown before the InGaAs separate confinement heterostructure (SCH) and quantum cascade active region. The InGaAs SCH was doped to give an electron concentration $n = 4 \times 10^{16} \text{ cm}^{-3}$. The SCH thickness was 0.3–0.5 μm , depending on wavelength and optimized through waveguide simulations to maximize the spatial overlap between the QC active region and the fundamental guided mode. Likewise, the upper cladding layer is similarly thick, to minimize the loss arising from the plasmon-enhanced confinement top layer (500-nm InP:Si with $n = 5 \times 10^{18} \text{ cm}^{-3}$ for the $\lambda \sim 8 \mu\text{m}$ structures, and $n = 1 \times 10^{19} \text{ cm}^{-3}$ for the $\lambda \sim 5 \mu\text{m}$ structures) and metal contact. To reduce the series resistance, the interfaces between the InGaAs SCH and the InP cladding layers comprise a step-graded InGaAsP layer.

During growth, the reflectance was measured in-situ, using a red (650 nm) laser in a normal-incidence geometry. An example of the in-situ reflectance is shown in Fig. 2, which shows the reflectance for several stages of the QC active region growth. The growth of each InGaAs and AlInAs layer is easily observed due to the refractive index change at each interface. The observation of this fine detail indicates that the surface is very smooth and the interfaces are abrupt; we also found from observing the *in situ* reflectance that the growth was very stable over the several hours required to grow the QC active region.

The structural quality of the QCL samples was evaluated by x-ray diffraction (XRD) and transmission electron microscopy (TEM); these techniques were also used to compare MOCVD growth parameter variations such as growth rate and interfacial growth interruptions. Accordingly, Fig. 3 shows the measured (004) double-crystal x-ray diffraction spectrum of two QCLs,

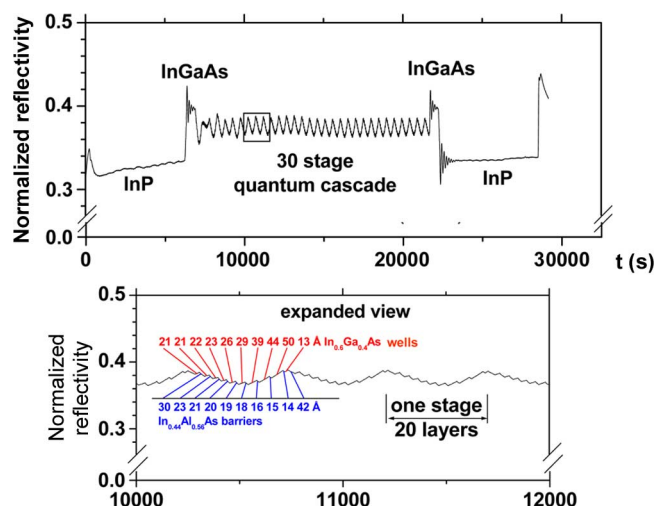


Fig. 2. Reflectivity signal during growth of a QC laser in the MOCVD reactor. Detail of active region growth is enlarged (below) to show the growth details of each single layer in the active region.

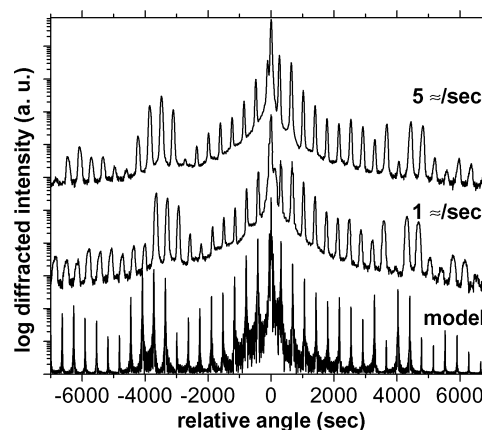


Fig. 3. Comparison between simulations and x-ray diffraction spectra of the fast- and slow-grown bound-to-continuum QCL measured along the (004) crystal direction. The curves are shifted for clarity. No significant change in wavelength emission was observed but 30% deterioration in laser performance was recorded.

one grown at the slow rate of 0.1 nm/sec, the other at a fast rate of 0.5 nm/s, in comparison to the simulated spectrum (bottom). The satellite reflections are clearly visible, indicating the presence of a periodic structure. The comparison between the XRD patterns of the fast- and slow-grown QCLs clearly show very similar diffraction spectra, with no noticeable degradation of the crystal quality as the growth rate changes, and an excellent run-to-run reproducibility of the structure.

For both samples in Fig. 3, the zeroth order peak due to the periodicity of the superlattice is very close to the InP substrate peak, which indicates only a slight weighted-average lattice mismatch in the structures. The average length of the QC stages can be deduced from the spacing of the satellites in the spectra: here the period of the active region is 49.3 and 49.7 nm for the slow- and fast-grown structures, respectively, which is in both cases slightly thinner than the targeted thickness. Finally, since the satellite peaks are produced by coherent reflections from each stage, their width is affected by any fluctuations in the deposition rate and composition that occur during the growth.

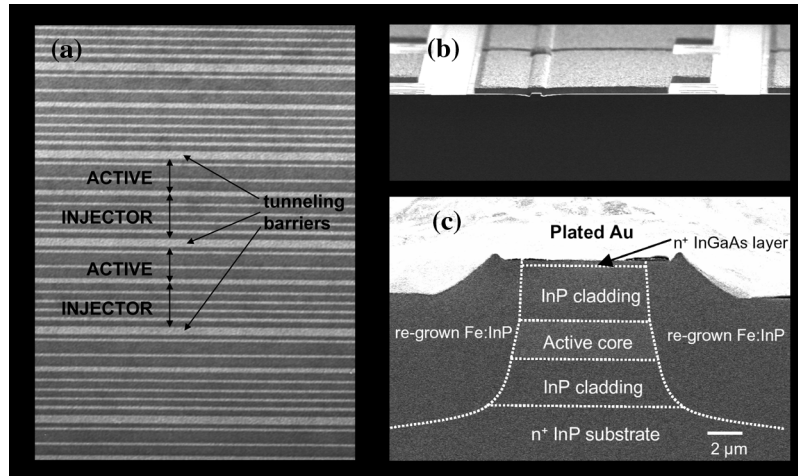


Fig. 4. (a) TEM picture of a partial section of the active region in a 3-quantum well active region QC laser. (b) SEM image of the finished device. (c) Close-up of the laser facet showing the buried heterostructure processing details.

Satellite peak widths as narrow as 15 arc seconds have been measured, approaching the system resolution of 12 arc-second. This indicates the growth is very stable over the 4–5 hours required to grow a typical QCL active region at the slow rate by MOCVD.

To further investigate the interface quality, we performed transmission electron microscopy (TEM) of the active region, as shown in Fig. 4(a) for a lattice-matched AlInAs-GaInAs QCL grown by MOCVD at a slow rate of 0.1 nm/s., with 5-s c growth interruptions at all interfaces. Observations were made with a JEM-4000EX high-resolution electron microscope operated at 400 keV. Samples were viewed in bright-field mode at or close to the common [110]-type projection. Clearest differentiation between the various layers was achieved using a small objective aperture. The TEM image confirms the good quality of the interface abruptness that can be achieved by MOVPE. Furthermore, TEM revealed no significant difference in the interface abruptness, comparing fast- and slow-grown (0.1 and 0.5 nm/s, respectively) QCLs. Similarly, there were no significant differences in quality for structures grown continuously compared to those grown with growth interruptions at all interfaces.

The laser threshold current and slope efficiency of QCLs whose interfaces were formed by these different techniques were also compared. Generally, roughly comparable QCL performance was obtained for structures grown continuously compared with those whose growth incorporated interruptions at all interfaces. This is in qualitative agreement with the structural characterization. Nevertheless, in contrast to the TEM and XRD comparisons of the various growth techniques, which indicated no apparent difference in interface quality, the QCL performance did reveal differences when fast and slow growth were compared. Namely, the threshold current was higher and slope efficiency lower, for structures grown at the higher rate. This might indicate some more subtle differences in the structural quality of the materials grown at a fast rate, which were not resolvable with TEM or XRD. On the other hand, other possibilities for the degraded performance of the fast-grown QCLs include higher background oxygen concentration in the

fast-grown heterostructures, since the V:III ratio could not be made as high for the fast growth; and the critically-important silicon doping calibration was not optimized for the fast-growth rate.

Shown in Figs. 4(b) and (c) is also the scanning electron microscope (SEM) picture of a finished device and a close-up of its front facet, after fabrication as buried heterostructure (BH) waveguide. The active region is clearly visible in the middle of the waveguide (light-colored area) and is surrounded by low-doped InP cladding layers (top and bottom) and by insulating InP layers (sides). The latter have been re-grown by MOCVD after ridge waveguides were etched by a combination of dry and wet etch into the material. InP re-growth was followed by metal contact deposition on top and on the back of the device, and in addition several microns of gold plating was deposited on the top side to further enhance the thermal dissipation capabilities. The devices were mounted epilayer-side up on a copper heat sink and micro-bonded to a contact pad conveying the bias current.

The active region of the devices presented here is based on three different types of designs that have been widely used in the literature and have been chosen to directly compare these MOCVD-grown lasers with previous results. Fig. 5 illustrates schematically three variations (insets) around the QC laser operating principle. In general, the structure is formed by alternating active and relaxation/injection regions [Fig. 5(a)]. The active region is where the optical transition takes place, while the “relaxation/injection” regions have the dual purpose of collecting carriers from the previous active region and injecting them into the following one.

A first optimized scheme for the active layers is the so-called “three wells vertical transition” [25] [Fig. 5(b)], where the active region consists of two coupled wells, plus a third one that favors injection into the initial state of the laser transition. The population inversion is generated by resonant optical phonon depletion of the lower laser level, since the two lowest active region states (E_0 and E_1) have an energy splitting corresponding to the longitudinal optical phonon energy. The injection of carriers into the upper laser level (level E_2) starts when the electric field is large

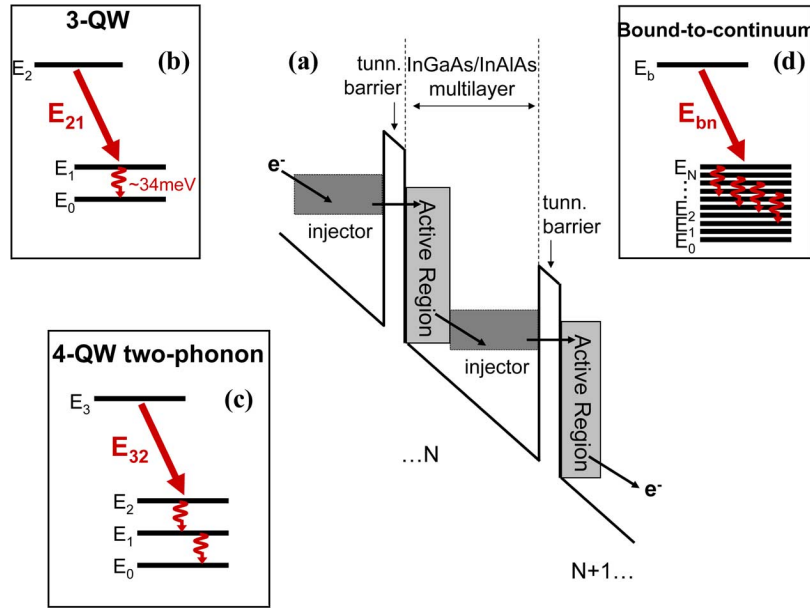


Fig. 5. Schematic illustration of QC laser energy band diagram and of the different active regions commonly employed in QC laser design. Horizontal lines represent electronic energy states, while shaded areas in the injector region represent minibands of states.

enough to allow for the carriers to be injected from the lowest energy states of the previous injector to the E_2 level of the following active region. The injection barrier is optimally designed to achieve hybridization between the upper laser level and the injector ground state in order to ensure a large dynamic range while limiting scattering to lower levels of the active region and maintaining a high oscillator strength of the laser transition [27].

More recent active region designs, like the dual-phonon [19] and the bound-to-continuum [28] shown in Fig. 5(c) and (d), have been specifically improved to have a more efficient depletion of the lower laser level. This is achieved by creating multiple states and therefore multiple relaxation channels so that: 1) the carriers effectively cool down to the injector's ground state after stimulated emission and 2) there is a limited back-filling of electrons from the injector into the lower laser level. The latter can be a problem particularly at high temperatures due to the larger high-energy portion of the electronic population distribution. As a result, the dual-phonon (4QW) and bound-to-continuum (BtC) schemes are the most suitable for high-performance RT operation.

Different active region designs yield different gain characteristics. This can be shown by comparing sub-threshold luminescence spectra measured at the same temperature for different materials. As shown in Fig. 6, the RT luminescence lineshapes of a three-quantum-wells vertical transition (3QW) and of a BtC active region have a considerably different FWHM, of 19 and 33 meV, respectively. This makes the BtC devices more suitable for use in applications where wide range tunability is an important requirement. Results will be shown later in this article on external cavity based widely tunable sources.

III. PULSED-MODE LASER OPERATION

In order to understand the performance of a semiconductor laser, it is important to recall the expression for the threshold condition (gain equal to the optical losses) and for the external

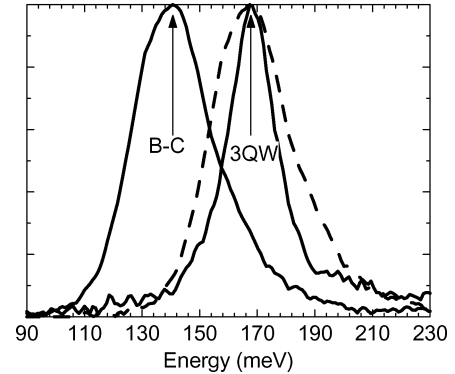


Fig. 6. Electroluminescence signals from bound-to-continuum (BtC) and 3-quantum-wells (3QW) active region materials. Dashed line is the horizontal translation of the BtC spectrum to overlap with the 3QW peak for direct comparison of the emission width.

differential quantum efficiency per facet. They read respectively as [29]:

$$g_{th}\Gamma = \alpha_w + \alpha_m \quad (1)$$

$$\frac{dP}{dI} = \frac{h\nu}{2q} \frac{\eta_i \alpha_m}{\alpha_m + \alpha_w} \quad (2)$$

where g_{th} is the material gain coefficient, Γ is the mode confinement factor, $h\nu$ is the emission energy, q is the electron charge, η_i is the device internal efficiency, P the total output power, α_w is the waveguide loss, and α_m is the mirror loss. The latter is defined as

$$\alpha_m = \frac{-\ln R}{2L} \quad (3)$$

where R is the reflectivity of the facets assumed to be equal for both ends of the waveguide and L is the laser cavity length, defined by the cleaved facets. In (2), it was assumed that there

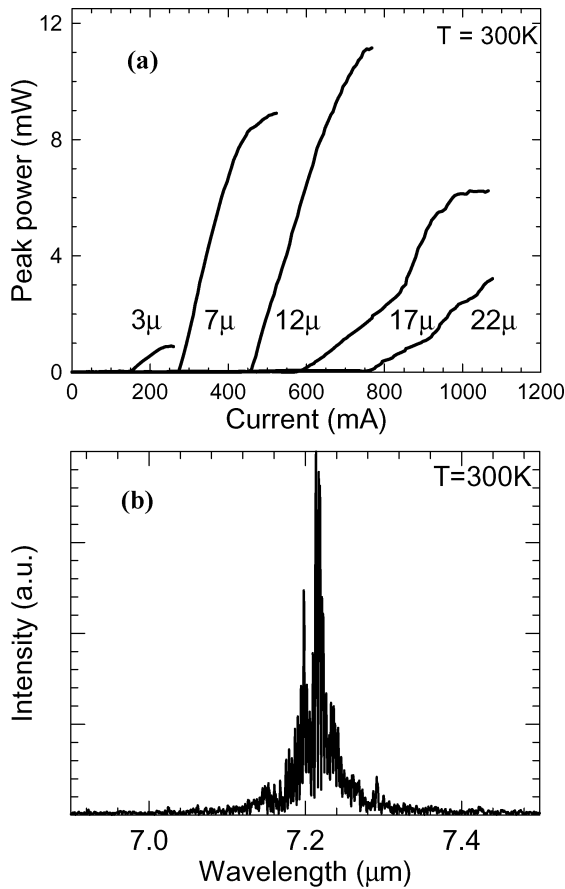


Fig. 7. (a) Optical power versus current characteristics of 3QW laser devices with different ridge widths. The curves have been selected after a set of devices had been tested per each width. Each curve is representative of the typical device behavior for each width. Devices widths are (from left to right): 3 μm , 7 μm , 12 μm , 17 μm , 22 μm . (b) Typical spectrum of the 7- μm wide device above threshold, measured at 300 mA and a duty cycle of 1%. All devices were $L = 2$ mm long.

is negligible population in the final state of the laser transition. For QC lasers the gain coefficient is given by [30]

$$g_{th} = \tau_3 \left(1 - \frac{\tau_2}{\tau_{32}} \right) \frac{4\pi q z_{32}^2}{\lambda_0 \epsilon_0 n_{eff} L_P} \frac{J_{th}}{2\gamma_{32}} \quad (4)$$

where $\tau_{3/2}$ is the total upper/lower laser level lifetime, τ_{32} and z_{32} are the 3-2 transition lifetime and dipole matrix element, while $2\gamma_{32}$ is the transition linewidth, J_{th} is the threshold current density, L_P is the thickness of one active stage and n_{eff} the effective refractive index.

RT pulsed operation characteristics of QC devices are shown in Fig. 7(a). The measured devices are based on a 3QW active region designed for emission at $\lambda = 8 \mu\text{m}$ [25]. In this case, differently from the reference design of *Gmachl et al.*, the active region doping is kept to $1 \times 10^{17} \text{ cm}^{-3}$ and the waveguide structure has thicker InP claddings. The active region was grown in-between two 0.5 μm -thick InGaAs waveguide core layers and two outer 3 μm -thick InP claddings. The InGaAs and InP layers are doped to 2×10^{16} and $1 \times 10^{17} \text{ cm}^{-3}$, respectively. The top layers are capped by a highly doped ($n = 5 \times 10^{18} \text{ cm}^{-3}$), 0.5 μm -thick InP layer for plasmon-enhanced confinement [31] and a thin InGaAs contact layer.

Typical optical power versus current (L - I) characteristics in Fig. 7(a) are for different device widths, ranging from 3 to 22 μm . The active region size is defined by dry etching and the ridge waveguide is then buried under a $\sim 5 \mu\text{m}$ -thick re-grown InP layer doped with Fe for electrical insulation. The top of the device is covered with a 5- μm -thick plated gold contact for enhanced thermal dissipation. Devices are all cleaved to the same cavity length ($L = 2$ mm). Devices are mounted epi-side up on copper heat spreaders.

Wider stripes are characterized by a larger threshold current, while the slope efficiency does not always increase as function of laser width. In addition, some of the L - I curves for wider stripes show kinks and changes in slope at high currents, which is a consequence of their multimode behavior in the lateral direction. A typical spectrum for devices operated in pulsed mode at $T = 300$ K is displayed in Fig. 7(b). The emission is centered around 7.21 μm and shows several longitudinal FP modes. The spectrum was recorded from a 7- μm -wide device operated close to threshold with a duty cycle of 1%.

For a finer analysis of the L - I characteristics, Fig. 8 displays the threshold current densities and the slope efficiencies of the same lasers of Fig. 7 as function of device width. The threshold current density does not change significantly with device width above 7 μm , which indicates that waveguide losses do not decrease significantly beyond this point. For widths smaller than 7 μm instead, the threshold current density increases considerably. Very small area devices with 3- μm width have on average a current density threshold 45% higher than the devices of 7 μm and above.

The increase in threshold current density is partially due to a smaller overlap factor (Γ) of the optical mode as the laser waveguide width becomes comparable to the wavelength of the laser emission in the material ($\lambda/n \approx 2.3 \mu\text{m}$). A reduction in the overlap factor has a twofold effect on the threshold current density: it contributes to lowering the peak modal gain of the laser, and it increases waveguide losses. The higher losses originate from having a larger fraction of the optical mode outside of the gain region, and in particular from the increased mode overlap with the highly absorbing plasmon confinement layer and top metal contact. Both effects lead to higher threshold currents that can therefore be significantly affected by small changes in Γ . In addition, higher losses in narrow lasers can be originated by a stronger interface scattering along the etched lateral walls of the cavity, where imperfections due to surface roughness and re-growth defects can significantly increase optical losses.

The slope efficiency in Fig. 8(b) is maximum for laser widths between 7 and 12 μm . The decrease in laser efficiency at small widths, as for the increase in threshold current density, is due to the decrease in the overlap factor observed in narrow laser stripes. The decrease in efficiency for large widths can be explained by an increase of the average active region temperature due to the much higher currents needed for broad area devices. The result is an optimal trade-off in the laser width in the range 7–12 μm .

The three different sets of curves in each panel of Fig. 8 correspond to different injector region doping. The doping levels considered in these measurements are $5 \times 10^{16} \text{ cm}^{-3}$, $1 \times 10^{17} \text{ cm}^{-3}$, and $2 \times 10^{17} \text{ cm}^{-3}$. Changing the doping from

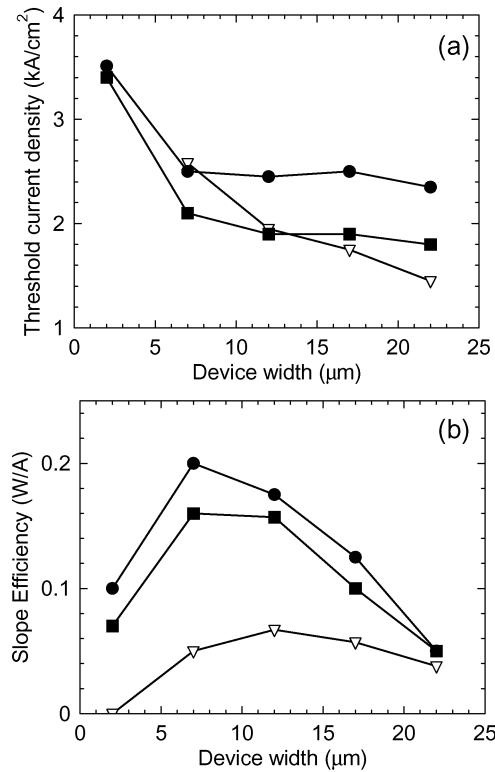


Fig. 8. Pulsed threshold current densities (left) and slope efficiencies (right) as a function of device width for different injector region doping at RT ($T = 300$ K). Dots: $n = 2 \times 10^{17} \text{ cm}^{-3}$, squares: $n = 1 \times 10^{17} \text{ cm}^{-3}$, triangles: $n = 5 \times 10^{16} \text{ cm}^{-3}$.

1×10^{17} to $2 \times 10^{17} \text{ cm}^{-3}$ increases the threshold current density. In fact, optical waveguide losses increase with doping due to higher optical absorption by carriers in the active region. For doping below $1 \times 10^{17} \text{ cm}^{-3}$ the threshold current density does not improve sensibly, since below this point it is most likely dominated by losses due to the highly doped top waveguide layers and metal contact.

Lasers based on highly doped material show higher slope efficiency, although from the data in Fig. 8(b) the efficiency increase is only 25% for a 2X doping increase from 1×10^{17} to $2 \times 10^{17} \text{ cm}^{-3}$, since absorption losses increase with doping as well. On the other hand, devices with the lowest doping (open triangles in Fig. 8) have a significantly smaller slope efficiency and total power. The lasers with smallest width processed out of this material did not operate at RT.

In the limiting case where all doping electrons are injected into the active region states, the maximum operating current of QC lasers can be estimated as $J_{\text{max}} = eN_D/\tau$, where N_D is the doping sheet density and τ is the lifetime of tunneling into the upper laser level [27]. Thus, by reducing the injector region doping in an effort to lower lasing threshold currents, we also reduce the dynamic range available to the laser and so its output power. No laser action will occur if J_{max} is smaller than the threshold current density required to overcome optical losses [32]. The optimal injector region doping level is therefore determined by the optical losses on the low side, and by the desired optical power output on the high side.

This is particularly important for CW operation, and is mostly dependent on the user requirements in terms of operating cur-

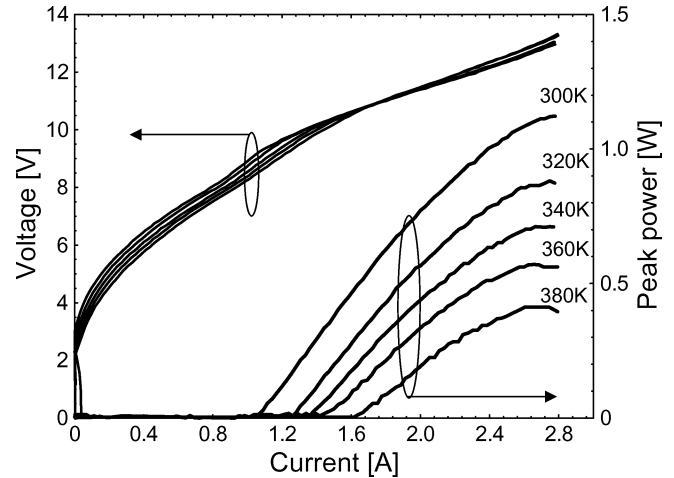


Fig. 9. Voltage-current (I - V) and optical power-current (L - I) characteristics of a bound-to-continuum device processed in $16 \mu\text{m}$ wide ridges measured at various heat sink temperatures: 300, 320, 340, 360, and 380 K, from the topmost to the bottom curve, both for the I - V and the L - I characteristics. The emission wavelength at threshold at 300 K is $\lambda = 8.9 \mu\text{m}$.

rents and maximum power outputs that are compatible with the system needs.

Figs. 9 and 10 show results from broad gain lasers processed as wide area devices. The two structures were grown following the BtC and the 3QW heterogeneous cascade (3QWH) schemes. In the former, the injector/active region stack is composed of 35 identical repetitions of the same active and injector layers described in [26]. In the latter instead, the stack growth included a variation of the active and injector layers thickness from the bottom to the top of the structure. The 3QWH active region consists of 36 stages grown in groups of 3. Within one group, the active region/injector layers are identical, while each group of stages has a slightly different thickness respect to the neighboring ones. Thicknesses decrease from the bottom to the top of the laser structure, in order to have stages designed for longer wavelength emission farther away from the top metal contact, as outlined in [33]. Thickness changes have been designed so that the expected emissions from neighboring groups of stages differ by about the half-width of the 3QW electro-luminescence spectrum at low temperature ($\sim 5 \text{ meV}$).

The two sets of devices show in both cases a high power output, as illustrated in Figs. 9 and 10. The BtC has a higher output power, reaching a maximum peak power of more than 1 W at 300 K. The 3QWH device is still capable of emitting 0.8 W of peak output power but it operates at higher currents due to the slightly larger area of this second set of devices ($18 \mu\text{m}$ wide versus the $16 \mu\text{m}$ wide BtC lasers). The 3QWH devices have an emission wavelength around $\lambda = 7.3 \mu\text{m}$, while for the BtC devices the center wavelength is $\lambda = 8.9 \mu\text{m}$.

If we compare the spectral emission bandwidth as function of injected current density, illustrated in Fig. 11, the BtC structure shows the broadest emission at high currents. On the other hand, the 3QWH structure has a behavior more similar to a supercontinuum emission [33]. The 3QWH lasers have a broader emission at low current densities and the bandwidth is quite flat over most of the current range. From the data in Fig. 11, it therefore appears that the BtC lasers have the broadest gain bandwidth,

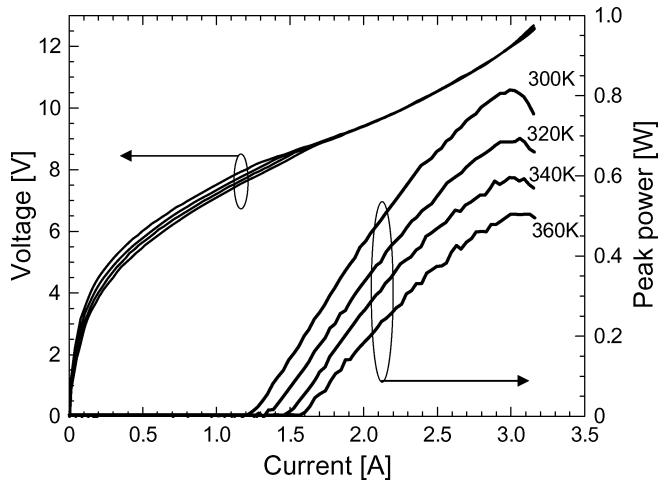


Fig. 10. Voltage-current (I - V) and optical power-current (L - I) characteristics of a 3-well-heterogeneous cascade device processed in $18\text{-}\mu\text{m}$ wide ridges measured at various heat sink temperatures: 300, 320, 340, and 360 K, from the topmost to the bottom curve, both for the I - V and the L - I characteristics. The emission wavelength at threshold at 300 K is $\lambda = 7.3\text{ }\mu\text{m}$.

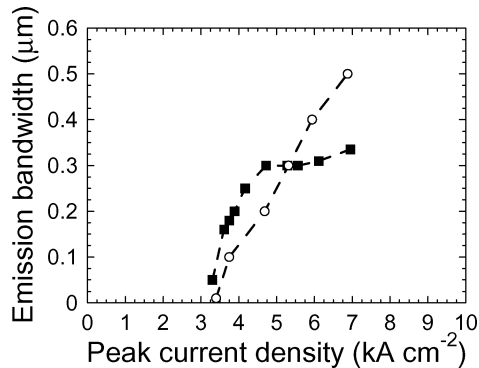


Fig. 11. Laser emission bandwidth as a function of the injected current densities for the B-C (circles) and the 3QWH (full squares) devices at RT ($T = 300\text{ K}$). The laser cavity length is $L = 2\text{ mm}$ for both devices.

while the 3QWH structures have a more uniform gain across the emission spectrum. In optimized designs of the 3QWH active gain media, the thresholds for laser action at different emission wavelengths should be close enough so to have emission over the whole spectrum within all of the laser dynamic range. A combination of the BtC and 3QWH approaches will eventually be the best compromise to realize broadband sources, as reported in [34].

A. Near-Field Mode Profiles

The mode profile and its stability as a function of pumping current are crucial for applications in which the output of a QC laser needs to be coupled into an optical fiber or an external cavity. We measured the near-field mode profile of BH devices using an atomic force microscope (AFM) operated in tapping mode. A sketch of our experimental setup is shown in Fig. 12. The QCLs were operated in pulsed mode (repetition rate $500\sim 800\text{ kHz}$, pulsewidth 125 ns) at RT. The AFM tip was used to scan the laser facet, scattering light from the near-field into the far-field, where it was collected by a ZnSe lens and focused with a second one on a liquid nitrogen cooled HgCdTe detector.

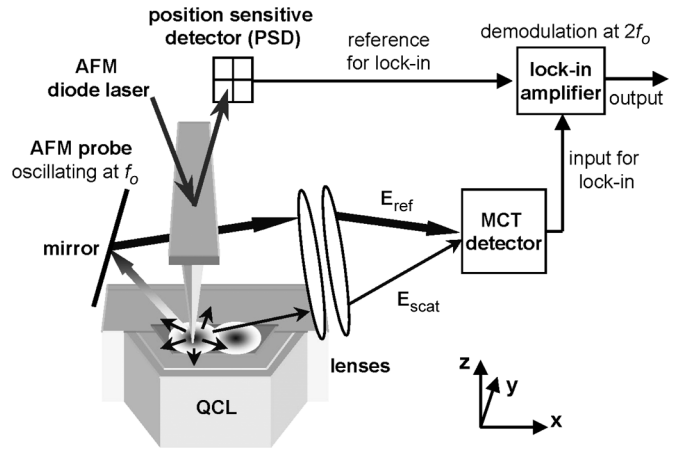


Fig. 12. Experimental setup consisting of a conventional AFM operated in tapping mode, used to obtain simultaneously the topography of the QCL facet and the near field images of the laser transverse modes. The light scattered by the AFM tip is focused on a liquid nitrogen cooled detector. The near field of the laser emission is measured by lock-in detection at twice the cantilever oscillation frequency. This configuration corresponds to an apertureless near-field scanning optical microscope.

This configuration corresponds to that of an apertureless scanning near-field optical microscope (a-SNOM) [35], [36]. This technique was recently used to image the longitudinal modes of so-called air-waveguide QC lasers [37] and the near field of an optical antenna built on the facet of a near infrared diode laser. Note that the interference between the near field scattered by the apex of the AFM tip and the light reflected from the mirror, which also originates from scattering by the tip, enhances the detection sensitivity.

The signal from the HgCdTe detector was fed into a lock-in amplifier. The cantilever oscillation frequency f_0 (typically 40 to 80 kHz) was significantly lower than the current pulse repetition rate used to drive the QCL and the lock-in detection was carried at twice f_0 in order to maximize the contribution originating from the near-field [38]. The topography and the near-field emission of the QCL were measured simultaneously. Small markers sculpted directly on the laser facet with focused ion beam (see SEM image in Fig. 13) allowed the position of the laser active core to be precisely determined with respect to the features observed in the near-field images.

Figs. 13(a) and 14 show the near field images obtained at different pumping current with BH QCLs with different ridge width. The devices used in the present experiment are similar to the ones described in Sections I and III. The optical mode emitted by the narrowest device ($\lambda = 5.29\text{ }\mu\text{m}$, active region width: $3\text{ }\mu\text{m}$, see inset in Fig. 13a)) corresponds to the fundamental mode TM_{00} while in the case of the broader devices ($\lambda \sim 7\text{ }\mu\text{m}$, active region widths: 12, 17, and $22\text{ }\mu\text{m}$, see Fig. 14) higher order lateral modes were measured. All devices were 2 mm long. The characteristics of the near field measured for the $3\text{ }\mu\text{m}$ wide laser does not change over the entire dynamic range of the laser ($I = 0.25\text{ A}$ to $I = 0.5\text{ A}$). Two-dimensional mode simulations performed using a commercial software (COMSOL Multiphysics 3.3) show that only a single lateral mode is supported in this case, thus explaining the stability of the mode profile as the current is increased.

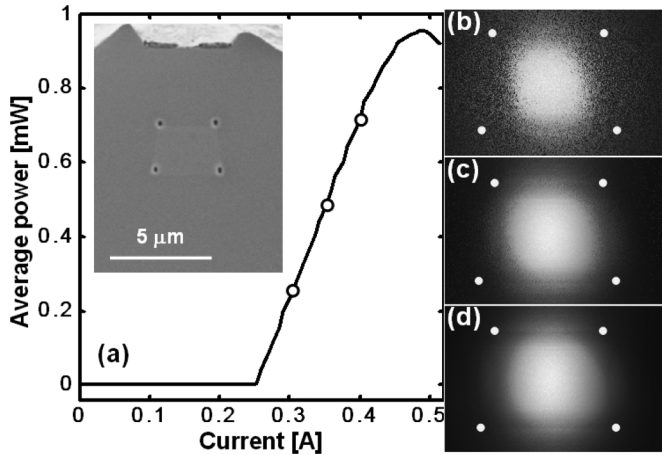


Fig. 13. (a) LI curve obtained at RT for a $\lambda \sim 5.29 \mu\text{m}$, $3 \mu\text{m}$ wide BH QCL operated in pulsed mode. The black points on the curve indicate the currents at which the near-field measurements were performed. Inset: SEM image showing the cleaved facet of the device. The four markers placed at the corner of the cross section of the active core are clearly visible. (b)–(d) Near-field optical images at different currents: (b) 300 mA, (c) 350 mA, and (d) 400 mA. The white dots indicate the position of the waveguide core.

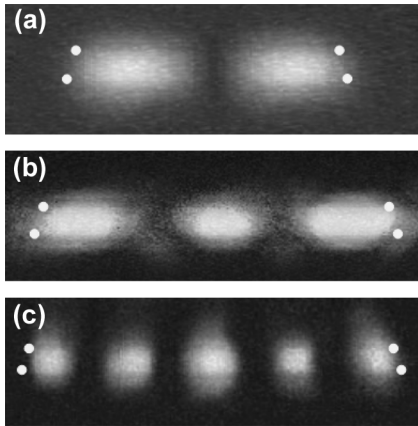


Fig. 14. Near-field optical images measured with three broad $\lambda \sim 7 \mu\text{m}$ BH QCLs operated in pulsed mode close to threshold. The devices used in this experiment are (a) 12, (b) 17, and (c) $22 \mu\text{m}$ wide respectively. The white dots indicate the position of the waveguide core. The data were recorded at RT with pulsewidth of 125 ns and repetition rates between 500 and 800 kHz.

Higher order lateral modes are supported when the ratio of the ridge width to the emission wavelength is increased. The mode patterns observed experimentally in wider lasers operated close to threshold can be assigned to TM_{01} [Fig. 14(a)], TM_{02} [Fig. 14(b)], and TM_{04} [Fig. 14(c)], for the 12, 17, and $22 \mu\text{m}$ wide lasers, respectively. In order to understand why these particular modes are selected, we calculated the confinement factor Γ as well as the waveguide and mirror losses (α_w and α_m) for all the possible modes supported by each ridge width. The mirror loss α_m was estimated by calculating the facet reflectivity for each mode using a simple ray optics model and the Fresnel formula, which is a good approximation in our case given that the active region is much wider than the wavelength in the laser material ($7 \mu\text{m}/3.3 \approx 2.1 \mu\text{m}$). The waveguide loss α_w was calculated with a simplified Drude model. The results obtained in the case of the $17 \mu\text{m}$ wide ridge are summarized in Table I.

TABLE I
CALCULATED VALUES OF THE OVERLAP FACTOR, MIRROR LOSSES, WAVEGUIDE LOSSES, AND THE FIGURE OF MERIT FOR THE VARIOUS LATERAL MODES SUPPORTED BY A $\lambda \sim 7 \mu\text{m}$, $17 \mu\text{m}$ WIDE DEVICE. THE LINE IN BOLD INDICATES THE MODE WHICH DOMINATES LASER EMISSION CLOSE TO THRESHOLD [SEE FIG. 14(b)]

Mode index	Overlap Factor Γ	Mirror losses α_m [cm^{-1}]	Waveguide losses α_w [cm^{-1}]	Figure of merit $(\alpha_m + \alpha_w)/\Gamma$ [cm^{-1}]
TM_{00}	0.52	6.17	6.76	24.8
TM_{01}	0.51	5.84	6.77	24.6
TM_{02}	0.50	5.25	6.85	24.3
TM_{03}	0.46	4.28	7.27	24.7
TM_{04}	0.34	2.57	13.87	48.2

In order to select the mode with the lowest threshold, we calculated in each case the quantity $(\alpha_m + \alpha_w)/\Gamma$ proportional to the threshold current. Our calculations show that the value $(\alpha_m + \alpha_w)/\Gamma$, is the lowest for the TM_{01} , TM_{02} , and TM_{04} modes in the case of 12, 17, and $22 \mu\text{m}$ wide devices, respectively, in good agreement with our measurements.

Note that beam steering of the far field pattern was observed as the current was increased well above threshold with the 12-, 17-, and $22\text{-}\mu\text{m}$ wide ridge BH devices. This phenomenon was already reported and modeled in interband laser diodes [39] and high-power QC lasers [40]. In devices showing far field steering, we observed asymmetric near field patterns. A detailed analysis of our measurements will be published elsewhere [41].

IV. CONTINUOUS-WAVE OPERATION

Fig. 15 shows the CW operation of 3QW lasers at RT. The lasers were processed as buried heterostructure ridge waveguides as discussed in [21] and were mounted epi-side up on a copper heat spreader bolted to a TEC cooled heat sink. Two sets of devices were investigated, with two different doping levels, $n = 1 \times 10^{17} \text{ cm}^{-3}$ and $n = 2 \times 10^{17} \text{ cm}^{-3}$, following the description of the previous section. The two upper panels of Fig. 15 illustrate the L-I characteristics of both types of device. The low-doped devices have lower threshold currents but also lower output power and a smaller dynamic range. Typical powers in the 10 mW's range were achieved at 300 K for both sets of devices, while at a heat sink temperature of 240 K powers of more than 100 mW were measured from the highly doped lasers. The low-doped devices have a power roll-off around $I = 0.5 \text{ A}$ and a maximum power at 240 K of 50 mW. All devices have an HR coating ($\text{Al}_2\text{O}_3/\text{Ti}/\text{Au}$) on the back facet, and their emission wavelength at 300 K is $7.2 \mu\text{m}$ [see inset of Fig. 15(a)].

The I-V characteristics are displayed in Fig. 15(c), where a larger differential resistance and operating voltage was measured for devices with lower doping. A smaller dose of doping electrons will in fact limit the total current at a given bias. The previously discussed equation $J_{\text{max}} = eN_D/\tau$ is a simplified description of carrier transport in the limiting case of optimal tunnel injection into the upper laser level. In general, the current density will have a more elaborate expression, where τ represents the total lifetime for all allowed electronic transitions from the injector states. The numerical calculation of this quantity can be quite complex and leads to an injection efficiency

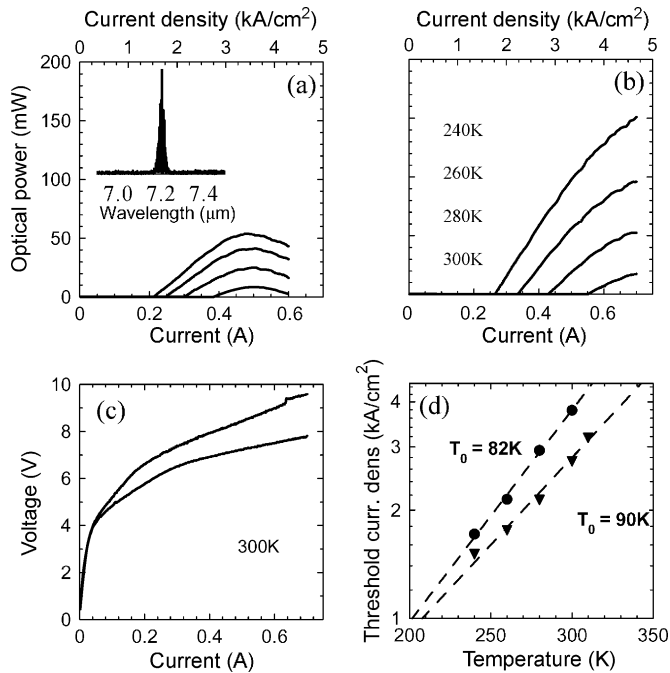


Fig. 15. CW characterization of 3QW samples doped to different levels and operated at various temperatures. (a) Optical power-current characteristics of the low doped sample at heat sink temperatures (from top to bottom) of: 240, 260, 280, and 300 K. (b) Optical power-current characteristics of the highly doped sample at heat sink temperatures (from top to bottom) of: 240, 260, 280, and 300 K. (c) voltage-current characteristics at 300 K for two different dopings. The topmost curve (from the low-doped sample) has the highest differential resistance. (d) Threshold current densities plotted as function of heat sink temperature. Dashed lines are numerical fitting lines following the expression: $J = J_0 \exp[T/T_0]$, where T_0 is the laser characteristic temperature. Inset: spectrum recorded at 300 K for the low-doped sample. The spectrum for the highly doped sample has similar characteristics and emission wavelength.

lower than 1 for transitions into the upper laser state [32]. The actual value of τ will depend on the electronic band structure, and therefore contains the dependence of J on the external bias voltage.

At the low doping levels typical of most QC laser designs ($N_D < 5 \times 10^{17} \text{ cm}^{-3}$) the band structure, and so τ , will not be significantly dependent on the carrier concentration. Thus, if we consider two identical active regions at the same bias voltage, the total current will be roughly proportional to N_D and therefore will be lower for devices with lower doping.

In addition, low-doped devices will have a narrower energy distribution (lower Fermi level) of electrons in the injection regions. This will allow for an efficient tunneling transport between the injector and active regions only within a small bias voltage range. As a consequence, low-doped devices have a limited dynamic range, evident from the comparison of Figs. 15(a) and (b).

If we compare the threshold current densities as function of temperature, we can extract the value of the laser characteristic temperature T_0 from the best-fit of the threshold data with the expression $J = J_0 \exp[T/T_0]$. The extracted values are 90 K for the low-doped devices and 82 K for the highly doped ones [see Fig. 15(d)]. These T_0 values are lower than what measured in devices optimized for RT operation like the 4QW and BtC lasers [42].

The characteristic temperature is an index of the laser sensitivity to temperature changes. Lasers that show a faster degradation of their performances for increasing temperatures usually are based on active region designs that are more sensitive to variations in the high-energy part of the electronic distribution. So-called “hot” electrons in the injection/relaxation regions [43] can reduce the injection efficiency and increase leakage currents into higher-lying conduction band states [31]. “Hot” electrons also contribute to the population of the lower energy level of the laser transition. Both effects reduce the population inversion and laser gain.

From our observations, consistent with previous literature, devices based on a 3QW designs have a limited RT output power and low value of T_0 , although their performance may be good enough for several spectroscopic applications.

In order to reach higher powers and higher operating temperatures, we grew and investigated [22]–[24] QC lasers based on BtC and in particular dual phonon (4QW) active regions. A summary of the results obtained with $\lambda = 8.4 \mu\text{m}$ and $5.3 \mu\text{m}$ devices based 4QW designs are shown in Figs. 16 and 17. The short wavelength laser was grown with a strain-compensated In-GaAs/InAlAs active region, as specified in [22]. Both sets of devices were processed as buried heterostructures and had a HR coating deposited on the back facet.

Fig. 16 shows the voltage-current and power-current characteristics for $\lambda = 8.4 \mu\text{m}$ devices with different width. The maximum power output is one order of magnitude larger than for the 3QW devices, reaching at a heat sink temperature of 300 K, maximum powers of more than 100 mW for a $3\text{-}\mu\text{m}$ -wide laser [Fig. 16(a)] and about 300 mW for a $7.5\text{-}\mu\text{m}$ -wide device [Fig. 16(b)]. Both devices operate at temperatures up to 400 K in continuous mode. A more complete discussion of these data can be found in [23].

The high power of these lasers is a combined result of multiple effects. The 4QW active region band structure, while improving RT operation and optimizing population inversion, also enhances the oscillator strength of the optical transition. This, together with the optimization of the doping distribution, leads to threshold current densities in the range of 1.5 to 2 kA/cm^2 as opposed to the 2.5 to 3.5 kA/cm^2 exhibited by 3QW devices. In this way, the electrical power used to drive the laser is reduced which helps lowering the active region temperature, leading to overall higher power efficiency in CW mode. In addition, lower thresholds allow for a wider dynamic range, therefore yielding a total power considerably larger than 3QW devices.

In the case of strained $\lambda = 5.3 \mu\text{m}$ material, similar performance has been achieved. Fig. 17(a) shows the characteristics for a $3\text{-}\mu\text{m}$ -wide device, reaching about 100 mW of output power at 300 K and 0.25 A. These devices show CW operation up to heat sink temperatures of 380 K. In the right panel of Fig. 17, we compared the optical power characteristics as function of current density for $3 \mu\text{m}$ wide devices of different length. In this case, longer devices have higher output power and slope efficiency.

From the data in Fig. 17(b) we find that the shortest ($L = 1.75 \text{ mm}$) and the longest ($L = 4.25 \text{ mm}$) devices have the largest threshold current densities while the lowest threshold corresponds to a length of $L = 3.25 \text{ mm}$. The larger current den-

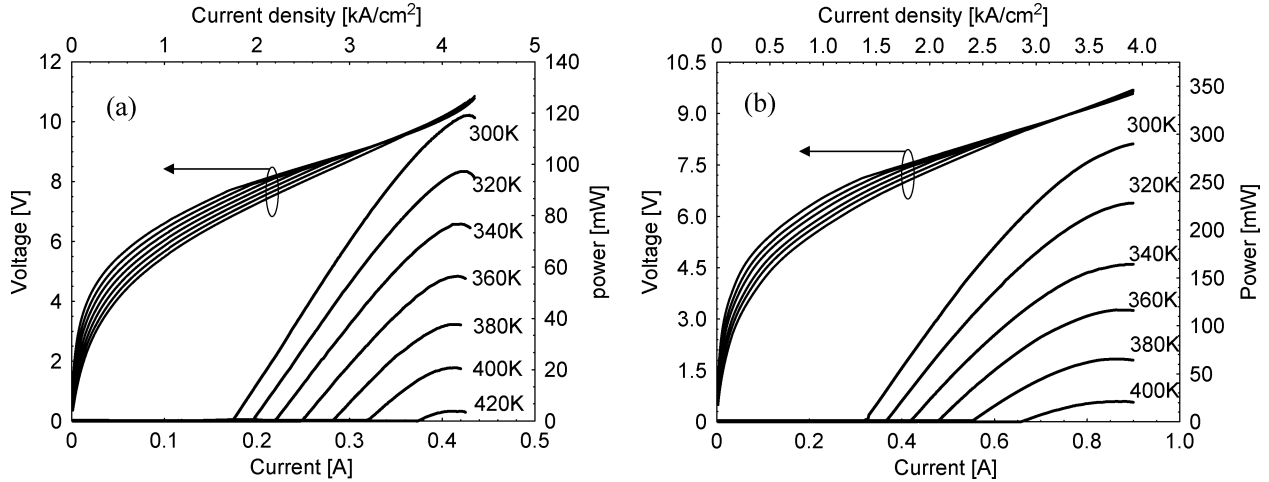


Fig. 16. CW characteristics measured at different heat sink temperatures for buried heterostructure devices with double phonon active region and emission wavelength of $\lambda \sim 8.4 \mu\text{m}$. (a) $3\text{-}\mu\text{m}$ -wide device. (b) $7.5\text{-}\mu\text{m}$ -wide device. The I - V characteristics are measured simultaneously with the L - I curves: higher currents at a given bias correspond to lower temperatures.

sities at smaller L can be understood in terms of higher mirror losses, being $\alpha_M = (L)^{-1} \log[(R_F R_B)^{-1}]$, where $R_{F/B}$ is the reflectivity of the front/back facet, assumed the same for all lasers. The increase in threshold current density for the longest devices instead can be ascribed to a higher average active region temperature due to the larger total current required for laser operation. This increase can be also partially due to the fact that longer devices may have a worse adhesion to the substrate since the soldering process can be more challenging for very long lasers.

Equations (1)–(3) in Section II can be used to estimate the optimal cavity length in order to extract the desired output power with the minimal amount of current, and therefore the best efficiency. This depends on an accurate estimate of the internal waveguide losses and on the control of the facet reflectivity by careful design of HR and AR coatings. [29] The lasers shown in Fig. 17 have a HR coating deposited on their back facets while the front facets are left uncoated. In this case, for example, to obtain a power of 20 mW, the shortest lasers (1.75 mm) could be operated with a current of only $I = 130 \text{ mA}$ (Fig. 17). For powers around 80 mW instead, the best efficiency would be obtained with the 3.25 mm lasers at $I = 0.2 \text{ A}$, while the longest lasers would need $I = 0.3 \text{ A}$ to emit the same power.

A. Spectral Characteristics

Many applications such as high-resolution gas spectroscopy require a single-frequency light source with a narrow linewidth. Narrow single mode emission can be obtained from distributed-feedback or external-cavity QC lasers operated in continuous mode. Fabry-Perot (FP) QC lasers have usually very broad spectra consisting of hundreds of longitudinal modes [44]–[46]. In this section, important details of the spectral characteristics of the high-power devices described in previous sections are discussed.

In Fig. 18(a), we show the dependence of the optical spectrum on the ratio between injected current and threshold current

for a two-phonon QC laser identical to the ones described in Section I (see Fig. 16). This 3-mm-long, $\lambda \sim 8.47 \mu\text{m}$ device was processed into a $3\text{-}\mu\text{m}$ -wide buried heterostructure laser and its back facet was left uncoated. This device, which was operated in continuous mode, is single mode close to threshold, but as the current is increased, many longitudinal modes appear and the spectrum broadens dramatically. Two humps clearly emerge in the envelope of the spectra at currents $\sim 20\%$ larger than the threshold current.

As shown in Fig. 18(b), the splitting observed experimentally is proportional to the square root of the laser output power. The Rabi frequency Ω_{Rabi} has the same power dependence, indicating therefore that coherent effects likely play a role in shaping the envelope of the laser spectrum [Fig. 18(a)]. We recently demonstrated that this is actually the case; an exhaustive explanation can be found in [45]. Simulations based on the full Maxwell-Bloch equations could reproduce the spectral envelope of the measurements shown in Fig. 18(a). It is important to point out that the model developed was based on a few parameters only and that both spatial hole burning as well as a saturable absorber had to be included in order to obtain a good agreement between theory and experiment.

The work presented in [47] and [48] established that the origin of the splitting observed for example in the data presented here is parametric gain due to the oscillation of the population inversion at the Rabi frequency. Even though modeling shows that the modulation of the inversion is only a small percentage, it greatly modifies the spectrum. This leads to additional gain positioned at multiples of $\pm\Omega_{\text{Rabi}}$ with respect to the maximum of the gain curve when the intracavity power is large. This coherent phenomenon resembles the one predicted by H. Risken, K. Nummedal and independently P. Graham, H. Haken almost 40 years ago, known as the RNGH instability [47], [48]. Note however that the RNGH instability was predicted to occur at nine times above the laser threshold. In our experiment instead, the threshold for the instability is much closer to the laser threshold, within a factor as low as 1.2. As explained in [42],

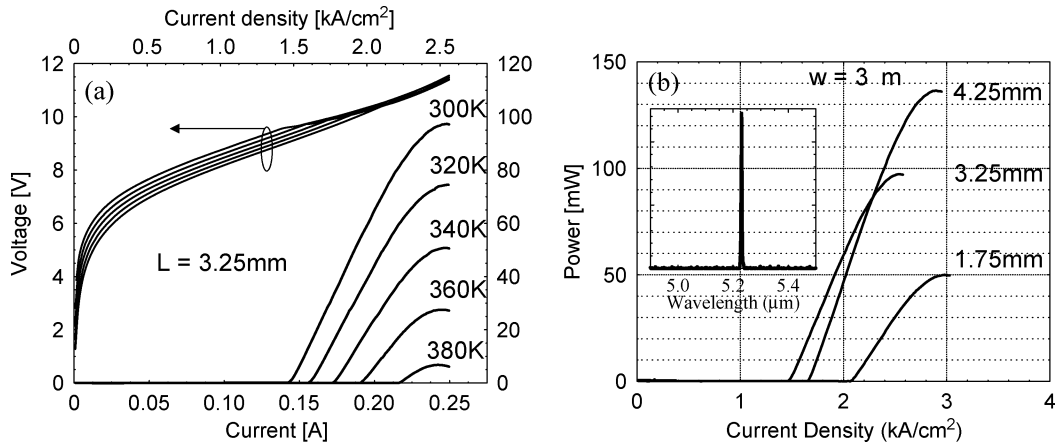


Fig. 17. CW characterization of a strained double phonon device processed as buried heterostructure. The emission wavelength at RT is $\lambda \sim 5.2 \mu\text{m}$ (see inset for a typical emission spectrum of a 3.25-mm-long device). (a) I - V and L - I characteristics for a $3\text{-}\mu\text{m}$ -wide, 3.25-mm -long device, measured at various heat sink temperatures in the range $T = 300\text{--}380\text{ K}$. The topmost I - V curves are the ones measured at the lowest temperatures. (b) Comparison of the optical power versus current density characteristics from devices of same width but different cavity length: $L = 1.75, 3.25$, and 4.25 mm , measured at $T = 300\text{ K}$.

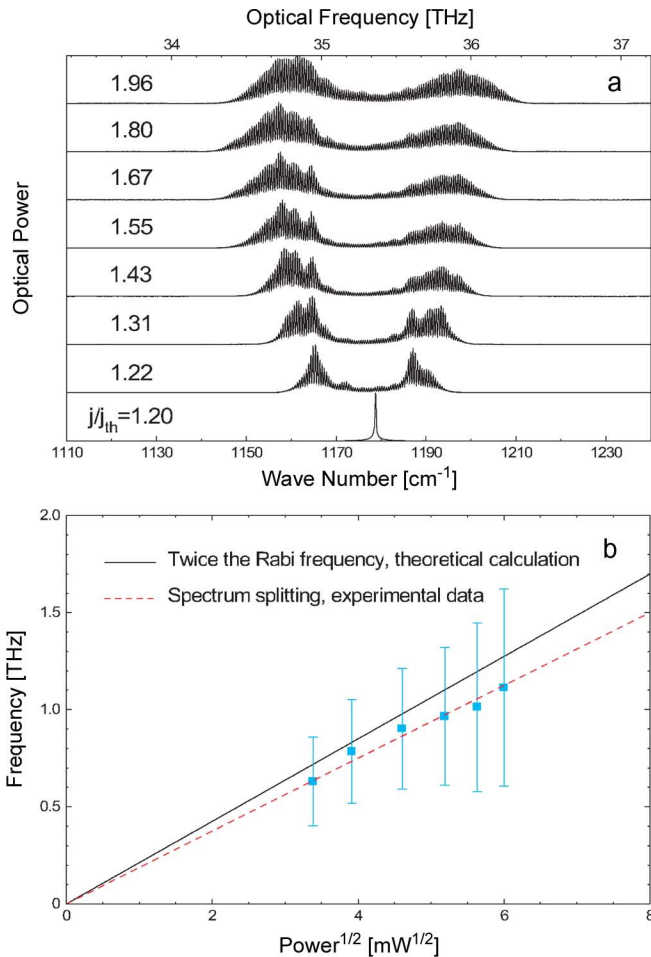


Fig. 18. (a) Optical spectra of a $\lambda \sim 8.47 \mu\text{m}$ BH device measured at 300 K in CW mode at different pumping ratios j/j_{th} . For $1 < j/j_{\text{th}} < 1.2$ the spectra are identical to $j/j_{\text{th}} = 1.2$. Note that the curves are shifted for clarity. (b) Spectral splitting and twice the Rabi frequency $\Omega_{\text{Rabi}}/(2\pi)$ versus the square root of output power collected from a single laser facet. The different quantities reported on the graph were deduced from the experimental data shown in (a). Dashed line is a least-square linear fit of the data.

this lowering is caused by the presence of a saturable absorber in the cavity.

For devices operating in the RNGH regime, i.e. with an intra-cavity power large enough to lead to the type of spectra shown in Fig. 18(a), the time-dependence of the laser output power is complex. The model described in [47] and [48] predicts indeed that trains of irregular pulses separated by roughly the gain recovery time are emitted. Under these conditions, the phase relation between both the pulses and the FP modes is also nontrivial. The optical spectrum of a QCL operated in the RNGH regime can vary significantly depending on the time scale considered. The measurements shown in Fig. 18(a) correspond instead to an average of the optical spectrum over many cavity round-trips. The output of these lasers driven by a DC power supply varies in time with a high average power, as seen in Fig. 18(b).

The theory developed in [42] and [43] illustrates how spatial hole burning (i.e., the formation of a gain grating due to the gain saturation and to the standing waves corresponding to the FP modes) contributes to the mode proliferation in the spectra such as in Fig. 18(a). This is very pronounced in QCLs due to the fact that the gain recovery time is much shorter than the grating diffusion time, in contrast to interband semiconductor lasers.

V. THERMAL ANALYSIS AND PERFORMANCE IMPROVEMENTS

Threshold currents and operating voltages are typically high in QC lasers, typically in the $0.2\text{--}0.7\text{ A}$ and $8\text{--}12\text{ V}$ range, respectively, thus easily leading to several (3–6) watts of electrical power. Hence, efficient dissipation of the generated heat is crucial to operate these devices in continuous mode at high temperature.

We performed thermal 2-D simulations using the commercial software COMSOL of a $\lambda = 8.4 \mu\text{m}$, $7.5 \mu\text{m}$ -wide BH QC laser capable of working in CW above 400 K . The performance of this particular laser is described in Section III and shown in Fig. 16. In our calculations, the temperature-dependent thermal conductivity of the different semiconductor layers (including the active region) as well as that of copper (submount), gold (electrical contact) and indium (solder) were taken from [18]. We tried in our model to reproduce realistically the Cu submount used in the experiment and the way the laser is attached to it. The Peltier cooler was replaced in our model by assuming a perfect

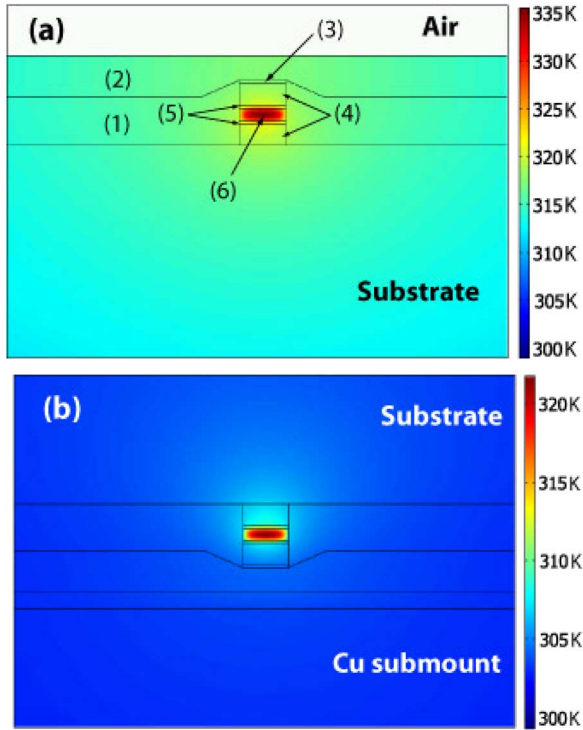


Fig. 19. (a) Results of the thermal modeling applied to a $\lambda = 8.4 \mu\text{m}$ 7.5 μm wide BH QCL mounted epi-side up. The electrical power-in corresponds to the experimental value obtained at threshold at 300 K in continuous mode. The symbols in the figure indicate the different elements entering in the geometry of the device: (1) regrown Fe:InP, (2) electroplated Au contact, (3) plasmon layer, (4) cladding layers, (5) InGaAs layers, (6) active region. (b) Temperature profile obtained for the same device mounted epi-down under the same electrical injection conditions.

heat sink at the bottom of the submount. The temperature at this boundary was defined taking into consideration that in the experiment, the temperature sensor was placed approximately 1 cm away from the sample; therefore, we made sure in our simulations that the temperature at this distance was 300 K.

Fig. 19(a) shows the calculated temperature profile obtained for injection conditions near laser threshold (corresponding to a total injected power of $P_{\text{el}} = 2.26 \text{ W}$), and at a heat sink temperature of $T_{\text{sink}} = 300 \text{ K}$. As expected, the temperature in the active region is significantly higher than 300 K. The spatial average over the active region cross section and the maximum temperature reached in the active region are $T_{\text{avg}} = 330 \text{ K}$ and $T_{\text{max}} = 335.5 \text{ K}$, respectively. From the ratio of the temperature difference $\Delta T_{\text{avg}} = (T_{\text{avg}} - T_{\text{sink}})$ and the electrical power P_{el} , we can extract an estimated thermal resistance at threshold for this device of 13 K/W. This number is actually in good agreement with the value measured experimentally (12 K/W) [23]. Note that our model predicts an average temperature as high as 432.6 K for the active region with an injected electrical power corresponding to the maximum of the $L-I$ curve ($P_{\text{el}} = 8.55 \text{ W}$) [23].

Flip-chip mounting is a widely used technique to improve the thermal management in semiconductor lasers. Fig. 19(b) shows the temperature distribution calculated for the same parameters and device geometry used to obtain the thermal map in

Fig. 19(a), but with the QC laser mounted epi-side down. Compared to the values obtained in the case of the epi-up laser close to threshold, the implementation of the flip-chip mounting technique leads to a decrease of the maximum core temperature by $\Delta T_{\text{max}} = 13.8 \text{ K}$. Similarly, the average temperature of the active region drops to $T_{\text{avg}} = 317 \text{ K}$ close to threshold (i.e. for $P_{\text{el}} = 2.26 \text{ W}$) and to $T_{\text{avg}} = 368.3 \text{ K}$, at the peak power of the $L-I$ -curve (i.e. for $P_{\text{el}} = 8.55 \text{ W}$).

These values correspond to a decrease in the temperature difference ΔT_{avg} of 40% to 50% in the case of flip-chip bonding. This is quite a large difference especially if we consider that the simulated devices have a BH waveguide that should minimize thermal effects. It is important to remark though, that the simulated case is an ideal case where the thermal contact at interfaces does not introduce additional resistance. In practice, flip-chip bonding is more challenging than epi-side up bonding and the actual improvement obtained could be significantly lower.

From the above calculations, it is difficult to quantify exactly how much the flip-chip mounting would improve the threshold current or the output power of the device. Because epi-down mounting leads to an estimated decrease of the average core temperature by about 14 K for $P_{\text{el}} = 2.26 \text{ W}$, one can expect the CW threshold current density for a flip-chip device at $T_{\text{sink}} = 300 \text{ K}$ to be roughly equal to the value obtained for an epi-up laser measured at $T_{\text{sink}} = 286 \text{ K}$. According to the data published in [23], this corresponds to a 13% decrease of the threshold current density. Likewise, the slope efficiency of a flip-chip device would not deteriorate as much. A maximum output power close to 400 mW at 300 K would therefore be anticipated for a flip-chip $\lambda = 8.4 \mu\text{m}$ 7.5- μm -wide BH QCL.

VI. ACCELERATED AGING

Preliminary accelerated aging measurements have been performed on CW operated BH devices similar to the one shown in Fig. 4. The devices were based on a lattice-matched InGaAs/InAlAs active region, and each was bonded to a separate AlN submount and mounted on a copper heat sink. No coating was applied to the device facets. The devices were biased in CW mode with stabilized current sources on a heat sink kept constantly at $T_{\text{H}} = 358 \text{ K}$ (85 °C) with typical operating currents. Samples of different area were biased with different currents in order to maintain approximately the same current density in each laser.

The details of the aging study for one of the investigated devices are displayed in Fig. 20. The operating current for this laser is $I = 0.4 \text{ A}$, corresponding to a current density of 2.5 kA/cm^2 . At this current level the device is capable of emitting 50 mW of continuous power per facet at $T_{\text{H}} = 293 \text{ K}$ (20 °C), while its maximum power output measured at $I = 0.5 \text{ A}$ is more than 100 mW. The maximum power output at $T_{\text{H}} = 20 \text{ °C}$ as a function of hours of operation at $T_{\text{H}} = 85 \text{ °C}$ was periodically measured and is displayed in Fig. 20. Power was measured with a calibrated thermopile detector without any optics so to avoid differences in collection efficiency. The average value of the maximum power output over time is 106 mW (dashed line in Fig. 20), with fluctuations of the measured intensity within 5%. These fluctuations can be partially due to differences in the measurement conditions such as the actual device temperature,

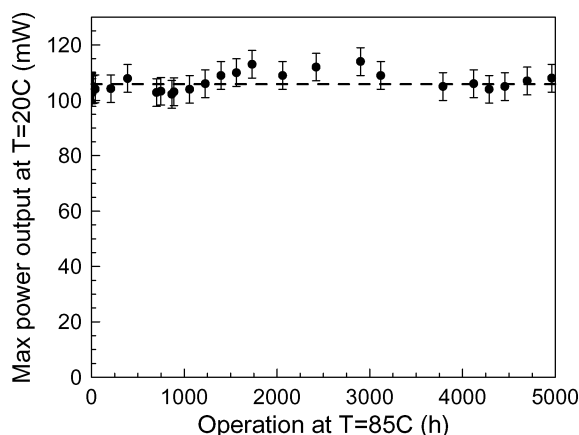


Fig. 20. Accelerated aging measurements from a typical device running continuously at a heat sink temperature of 85 °C with a bias current of 0.4 A. The device emits at $\lambda = 8.6 \mu\text{m}$ and was periodically tested at a heat sink $T = 20^\circ\text{C}$. The figure shows the maximum output power at 20 °C recorded as a function of hours of operation at 85 °C. Data courtesy of Argos Tech.

the detector calibration, or different background temperature effects.

For the sample shown in Fig. 20, no significant power degradation (i.e., 10% or more) is observed after almost 5000 h.

VII. APPLICATIONS

Infrared laser absorption spectroscopy (LAS) is an extremely effective tool for the detection and quantification of molecular trace gases. The demonstrated detection sensitivity of LAS ranges from ppmv and ppbv to even pptv levels depending on the specific gas species and the detection method employed [49], [50]. The spectral region of fundamental vibrational molecular absorption bands in the wavelength range from 3 to 24 μm is the most suitable for high-sensitivity trace gas detection. However, the usefulness of laser spectroscopy in this region is limited by the availability of convenient tunable laser sources. Real world spectroscopic applications require the laser sources to be compact, efficient, reliable and operating at near RT. Existing options include lead salt diode lasers, coherent sources based on difference frequency generation (DFG), optical parametric oscillators (OPOs), tunable solid-state lasers, quantum and interband cascade lasers. Sensors based upon lead salt diode lasers are typically large in size and require cryogenic cooling, because these lasers operate at temperatures of $< 90^\circ\text{K}$. DFG sources (especially periodically poled lithium niobate based bulk and waveguide) have been shown to be robust and compact [51], [52] enough for desktop-type applications but have limited mid-infrared output power.

The recent advances of quantum cascade (QC) and interband cascade (IC) lasers fabricated by band structure engineering offer an attractive new source option for ultra sensitive and highly selective, mid-infrared absorption spectroscopy [53]. As discussed in previous sections, the most technologically developed mid-infrared QC laser source to date is based on type-I intersubband transitions in InGaAs/InAlAs heterostructures. Both pulsed and CW, thermo-electrically cooled (TEC) distributed feedback (DFB) QC lasers possess the key characteristics such as narrow linewidth and high powers (tens

to hundreds of milliwatts in single-frequency operation) that make these devices effective in laser absorption spectroscopy. These characteristics allow the use of advanced spectroscopic detection techniques as well as the implementation of compact and robust trace gas sensor architectures. This applies specifically to QC laser sensor systems based on long/open path laser absorption spectroscopy [including remote sensing techniques such as light detection and ranging (LIDAR) or differential absorption LIDAR (DIAL)], cavity enhanced spectroscopy and photoacoustic spectroscopy. The large available wavelength coverage from $\lambda = 3$ to 24 μm with IC and QC lasers in the molecular fingerprint region allows the detection, quantification and monitoring of numerous molecular trace gas species, especially those with resolved rotational-vibrational spectra. Several applications which demonstrate the excellent potential of QC lasers as mid-IR spectroscopic sources are discussed below.

A. Chemical Sensing Based on Tunable Thermoelectrically Cooled CW Quantum-Cascade Lasers

High optical power and single-frequency operation with good spectral purity or wide tunability of the laser source are the most critical characteristics for chemical trace gas sensing using spectroscopic techniques. Single frequency operation is usually achieved by introducing a distributed feedback (DFB) structure into the QCL active region. Although state-of-the-art DFB QCLs show high performance and reliability, the ability to obtain the optimum emission wavelength for a desired target analyte is costly and the range of wavelength tuning of the emitted laser radiation is strongly limited by the wavelength tuning range of the embedded DFB structure. Typically, the maximum tuning range of DFB-QCLs achieved by changing the laser injection current is $\sim 2 \text{ cm}^{-1}$ and can be increased to $\sim 10 \text{ cm}^{-1}$ by varying the temperature of the QCL chip. However, the spectral width of the QCL optical gain profile is usually significantly broader than 10 cm^{-1} and therefore QCLs can provide in fact a much broader wavelength tuning range.

As previously discussed in Section II, the bound-to-continuum QC laser design first proposed by Faist *et al.* [28] and the heterogeneous QC structure first demonstrated by Gmachl *et al.* as a supercontinuum QCL [33], have been the most promising in terms of broadband emission, and have been further developed for wide single-mode-frequency tuning spectroscopic applications by Maulini *et al.* [34]. A luminescence spectrum of 297 cm^{-1} FWHM at RT was observed for $\lambda \approx 10 \mu\text{m}$ QCL devices employing bound-to-continuum transitions [54], while even broader gain profiles with FWHM of $\sim 350 \text{ cm}^{-1}$ were achieved in [34] using both concepts of heterogeneous quantum cascade structure based on two bound-to-continuum designs emitting at 8.4 and 9.6 μm , as briefly discussed in Section II. To take advantage of the broadband gain of such QCLs, an external cavity (EC) configuration can be used to obtain a single mode operation at any wavelength within the laser gain profile [55], [56].

A widely tunable QC laser spectrometer implementing a novel EC-QCL architecture for high-resolution spectroscopic applications and multi species trace-gas detection was recently demonstrated with a thermoelectrically cooled FP gain medium

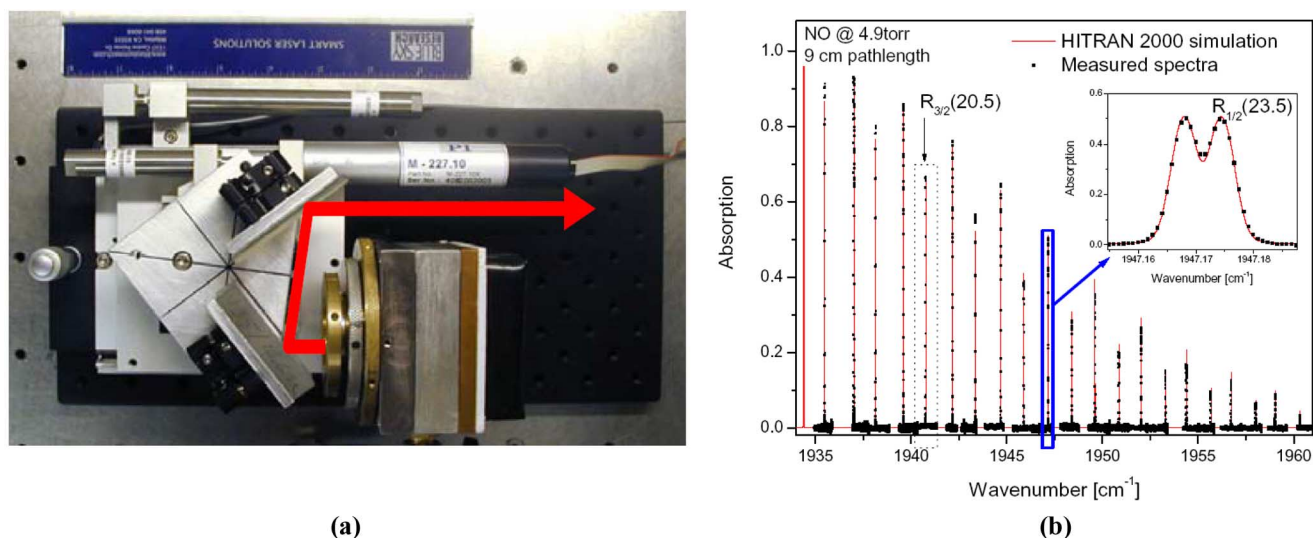


Fig. 21. (a) Photograph and (b) a 3-D mechanical model of a compact tunable external grating cavity QCL. (c) Nitric oxide absorption spectra simulated for a 1 ppm NO mixture at atmospheric pressure and open path of 286 m (in red) shown together with an external cavity-QCL tunability range. Atmospheric absorption caused by H₂O (mixing ratio = 0.006) and CO₂ (mixing ratio = 380 ppm) is depicted in blue. (d) Spectral measurements performed for NO lines, which are optimal for atmospheric measurements (the narrow QCL linewidth allows spectral resolution of $< 0.001 \text{ cm}^{-1}$).

operating in a CW mode at $\lambda \sim 5.28 \mu\text{m}$. The instrument depicted in Fig. 21(a) and (b) employs a piezo-activated cavity mode tracking system for mode-hop free operation. The mode-tracking system provides independent control of the EC length, diffraction grating angle and laser current. The QCL gain medium allowed a coarse laser frequency tuning range of $\sim 155 \text{ cm}^{-1}$ and a high resolution (better than 0.001 cm^{-1}) continuous mode-hop free fine tuning within a range of up to 2 cm^{-1} with a maximum available optical power of $\sim 11 \text{ mW}$. Wide wavelength tunability around $\lambda = 5.28 \mu\text{m}$ allows accessing most of the absorption lines within the fundamental vibrational band of NO as shown in the HITRAN simulation presented in Fig. 21(c).

A narrow laser linewidth of $< 30 \text{ MHz}$, which allowed resolving spectral features separated by $\sim 0.01 \text{ cm}^{-1}$ makes the EC-QCL an excellent light source suitable for high-resolution spectroscopic applications and multiple species trace-gas detection [see measurements performed for a NO gas sample at both atmospheric and reduced pressure of 10 Torr shown in Fig. 21(d)]. The flexibility of this arrangement makes it possible to use it with any QCL gain media without the need of an embedded DFB structure and at any mid-infrared wavelength without changing the EC configuration.

The use of a MOCVD grown buried heterostructure FP QCL gain medium operating at $\lambda = 8.6 \mu\text{m}$ in the above described EC-QCL sensor architecture resulted in considerably higher levels of optical output power. The maximum single frequency output power obtained in the EC-QCL configuration was 50 mW, which represents a significant improvement compared with results obtained in [55] using a previous version of this system.

B. Trace Gas Detection Based on Laser Photoacoustic Spectroscopy (PAS)

PAS, based on the photoacoustic effect, in which acoustic waves result from the absorption of laser radiation by a se-

lected target compound in a specially designed cell is an effective method for sensitive trace gas detection. In contrast to other infrared absorption techniques, PAS is an indirect technique in which the effect in the absorbing medium and not the direct light absorption is detected. Light absorption results in a transient temperature effect, which translates into kinetic energy or pressure variations in the absorbing medium via non-radiative relaxation processes that can be detected with a sensitive microphone. PAS is ideally a background-free technique, since the signal is generated only by the absorbing gas. However, background signals can originate from nonselective absorption of the gas cell windows (coherent noise) and external acoustic (incoherent) noise. PAS signals are proportional to the pump laser power and therefore the maximum detection sensitivity that can be realized by means of the PAS technique is most effective with high-power laser excitation. A sensitivity of 8 ppmv was demonstrated with only 2 mW of modulated diode laser power in the CH₄ overtone region [57], [58]. The implementation of high-power CW TEC QCL laser excitation in the fundamental absorption region leads to considerably improved trace gas detection sensitivity. The MOCVD-grown QC lasers based on buried heterostructure design, which offer high output power levels, are at this time the most promising QC mid-IR laser sources for PAS.

A recently introduced novel approach to photoacoustic detection of trace gases utilizing a quartz tuning fork (QTF) as a sharply resonant acoustic transducer was first reported in 2002 [59], [60]. The basic idea of quartz enhanced photoacoustic spectroscopy (QEPAS) is to invert the common PAS approach and accumulate the acoustic energy not in a gas-filled cell but in a sharply resonant acoustic transducer. A natural candidate for such an application is crystal quartz, because it is a low-loss piezoelectric material. Readily available quartz crystals are quartz tuning forks (QTF) intended for use in electronic clocks as frequency standards. QTFs typically resonate at $32\,768 (2^{15}) \text{ Hz}$ in vacuum. A typical

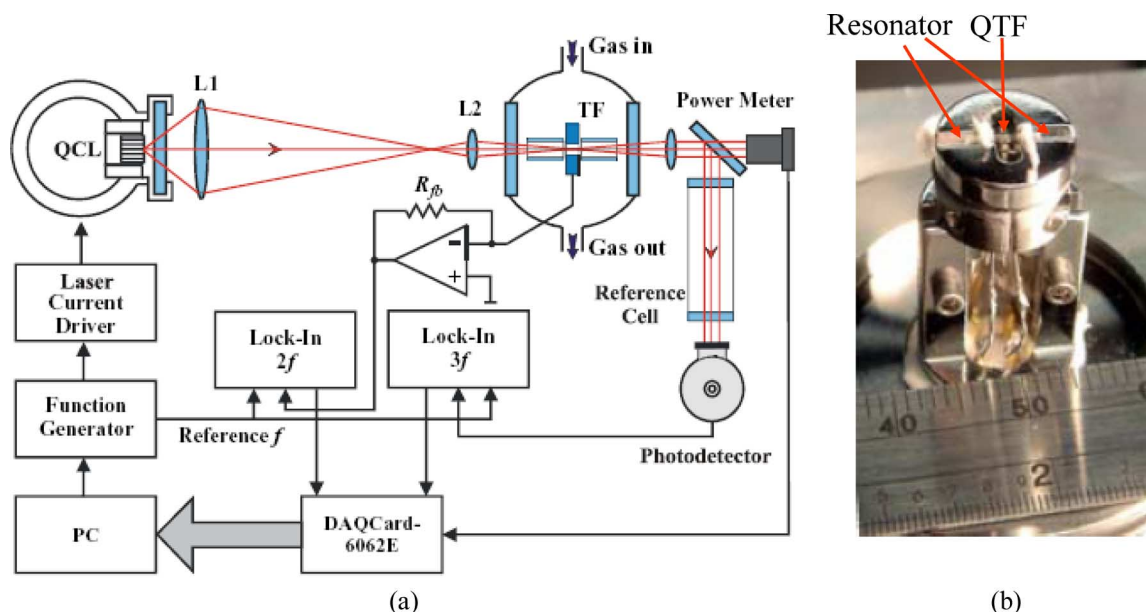


Fig. 22. (a) Schematic of a QCL-based quartz-enhanced photo-acoustic spectroscopy sensor platform showing a quartz tuning fork and acoustic micro-resonator. (b) Picture of a QEPAS absorption detection module consisting of QTF and micro-resonator.

sensor architecture is depicted in Fig. 22(a) together with a picture of a QEPAS absorption detection module (ADM) consisting of a QTF equipped with a micro-resonator as shown in Fig. 22(b). The laser radiation is focused between the prongs of the QTF and its wavelength is modulated at $f_m = f_0/2$ frequency or its intensity is modulated at $f_m = f_0$ frequency (where f_0 is the QTF resonant frequency) depending on the type of detection scheme used: a wavelength modulation or an amplitude modulation technique, respectively. The laser induced acoustic wave at f_0 becomes the driving force to excite the symmetric fundamental mechanical vibration of the QTF prongs (i.e., the two QTF prongs move in opposite directions). The electrical signal produced by this piezo-electrically active mode of vibration is measured using lock-in detection at f_0 . Spectral data can be acquired if the laser wavelength is scanned. To increase the effective interaction length between the radiation-induced sound and the QTF, a gas-filled acoustic resonator can be added similarly as in the traditional PAS approach. Sound waves from distant acoustic sources tend to move the QTF prongs in the same direction, which results in zero net piezo-current thus making this element insensitive to such excitation. Advantages of QEPAS compared to conventional resonant photoacoustic spectroscopy include QEPAS sensor immunity to environmental acoustic noise, a simple absorption detection module design, no spectrally selective element required, its being applicable over a wide range of pressures, including atmospheric pressure and its capability to analyze small gas samples, down to 1 mm^3 in volume. QEPAS sensor technology has already been demonstrated in trace gas measurements of 10 target analytes, including NH_3 [61], CO_2 [62], [63], N_2O [64], HCN [65], CO in propylene [66] and CH_2O [67]. A normalized noise equivalent absorption coefficient of $1.9 \times 10^{-9} \text{ cm}^{-1} \text{ W/Hz}^{-1/2}$ was measured to date using QEPAS [68]. An experimental study of the long-term stability of a QEPAS-based NH_3 sensor showed that the sensor exhibits very low drift, which allows long term data averaging

(>3 h) and thus leads to a significant improvement of the signal-to-noise ratio in concentration measurements.

Recently Wojcik *et al.* [69] reported the performance of an amplitude modulated (AM) $8.4\text{-}\mu\text{m}$ QC laser-based QEPAS sensor system that demonstrated the detection of broadband absorbing target species in the mid-infrared spectroscopic fingerprint region. Using a similar approach, we developed a QEPAS sensor employing an external cavity laser utilizing a MOCVD-grown FP BH QCL gain medium like the ones described in Sections II and III, targeting the broadband absorption spectrum of C_2HF_5 (Freon 125) at $\lambda \sim 1150 \text{ cm}^{-1}$. The laser source exhibits single-frequency tuning of 135 cm^{-1} . In this sensor a photoacoustic signal is generated by modulating the amplitude of the laser radiation with 100% modulation depth and a 50% duty cycle at the exact resonance frequency of the applied quartz tuning fork. The sensitivity of this sensor was determined both for single point measurement as well as in a broadband wavelength scan using a calibration mixture of 5 ppm Freon-125 A in dry nitrogen. With a laser frequency set to 1208.62 cm^{-1} , which corresponds to the maximum absorption of Freon 125 in this spectral region, a continuous concentration measurement was performed. An example of an AM-QEPAS signal of the Freon 125 calibration mixture recorded between several subsequent zero gas flushes is shown in Fig. (23a). A minimum detection limit (1σ) of $\sim 3 \text{ ppb}$ was calculated for these conditions based on the scatter of the background signal measurements. The power and measurement bandwidth normalized noise equivalent absorption coefficient (NNEA) of this sensor was determined to be $2.64 \times 10^{-9} \text{ W cm}^{-1} \text{ Hz}^{-1/2}$ for Freon 125. The applied CW TEC EC QC laser is able to provide $\sim 50 \text{ mW}$ of optical power. This translates into a minimum detection sensitivity limit for C_2HF_5 of $\sim 1.1 \times 10^{-7} \text{ cm}^{-1}$ for a $t = 1 \text{ s}$ averaging time and amplitude modulation with a 50% duty cycle.

AM detection of a broad band absorber at a single spectral point can only be performed for gas mixtures that do not con-

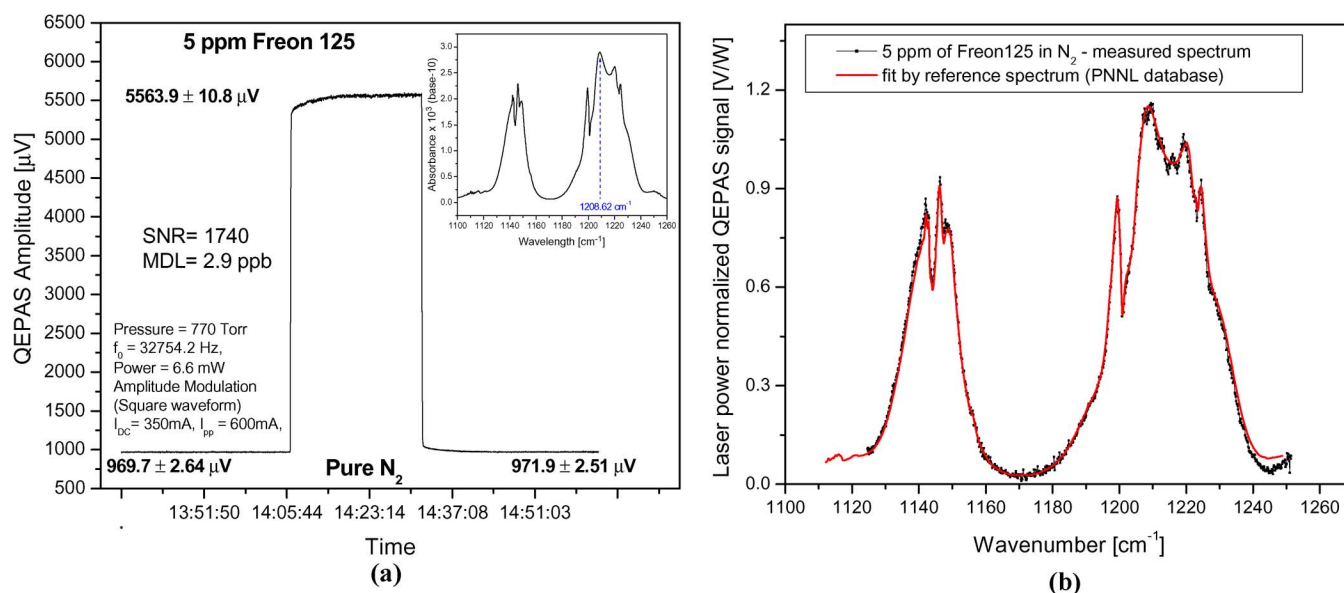


Fig. 23. (a) Freon 125A concentration measurement performed with a 8.6 μm QCL-based amplitude modulation—quartz enhanced photo-acoustic spectroscopy trace gas sensor system at the spectral location of a maximum absorption. The inset shows a spectral location of the laser frequency on the Freon 125 absorption spectrum. $\text{NNEA} = 2.55 \times 10^{-9} \text{ W cm}^{-1} \text{ Hz}^{-1/2}$. (b) Photoacoustic spectrum of Freon 125 measured between 1125 and 1250 cm^{-1} fitted by the reference spectrum from the spectral database.

tain species absorbing in the same spectral region. This inconvenience can be avoided by application of broadly tunable lasers, which can be tuned over a wide range of wavelengths and allows measurement of a unique spectral envelope of the target broadband absorption feature. EC-QCL seems to be an ideal tool for such application. Fig. 23(b) depicts a spectrum of the same calibration mixture (5 ppm of Freon 125 in N_2), which was recorded with our EC-QCL based AM-QEPAS system. Excellent agreement of a measured spectrum with a spectrum obtained from spectroscopic database (Pacific Northwest National Laboratory Infrared Spectral Library) was observed. This in combination with appropriate data acquisition processing and analysis methods (see [70]) allows concentration measurements with high molecular selectivity even in presence of spectrally interfering molecular species. The Freon 125 minimum detection limit at the level of ~ 4.5 ppb was calculated using a parameter-determination error yielded by the fitting process.

C. Trace Gas Sensing Using a High-Finesse Optical Cavity

Sensitive laser absorption spectroscopy often requires a long effective pathlength of the probing laser beam in media that are to be analyzed. Traditionally, this requirement is satisfied using an optical multipass cell. Such an approach can be difficult to implement in certain field applications, requiring compact gas sensor configurations. For example, a typical commercial 100-m pathlength multipass cell has a volume of 3.5 L. An alternative way to obtain a long optical path is to make the light bounce along the same path between two ultralow-loss dielectric mirrors forming a high-finesse optical resonator. An effective optical pathlength of several kilometers can be obtained in a very small volume. The light leaking out of such an optical cavity can be used to characterize the absorption of the intracavity medium. Presently a variety of techniques exists to perform high-sensitivity absorption spectroscopy in a high-finesse optical cavity

such as cavity ringdown spectroscopy (CRDS) [71], [72] or integrated cavity output spectroscopy (ICOS) [73], [74]. In these techniques the coupling efficiency of the laser radiation into the resonant cavity is extremely critical and determines the amount of light which can be collected by a photodetector placed after the absorption cell. In an off-axis ICOS (OA-ICOS) arrangement, in which the optical system is aligned in such a way that the maximum number of longitudinal and transverse modes is excited within the cavity, the typical optical throughput of the cavity is on the order of 0.1%. In this case, the system requires a very sensitive detector (usually cryogenically cooled) in order not to be limited by the detector noise floor. Therefore, these techniques can also benefit from the increased laser power available from CW, high-power QCLs, which results in substantial improvement of their detection sensitivity and/or allow to use less sensitive, but thermoelectrically cooled detectors, which is critical in a field-deployable gas sensor system.

A nitric oxide sensor based on a thermoelectrically cooled, CW DFB QCL laser operating at $\lambda = 5.45 \mu\text{m}$ (1835 cm^{-1}) and off-axis ICOS combined with a wavelength-modulation technique was developed to determine NO concentrations at the sub-ppbv levels that are essential for a number of applications, such as in medical diagnostics (specifically in detecting NO in exhaled human breath) and environmental monitoring [75]. Exhaled nitric oxide (eNO) is an important biomarker in many respiratory diseases [76] and the exhaled NO levels have been extensively studied in asthma cases. These measurements may be clinically useful in other chronic respiratory conditions, such as chronic obstructive pulmonary disease (COPD), particularly if the NO contributions are partitioned into alveolar and conducting airway regions. Exhaled NO levels generally range between 4 to 15 ppbv in healthy human subjects and 10–160 ppbv in subjects with untreated asthma when breath is collected at the standard 3 L/min, in accordance with the American Thoracic Society (ATS) recommendations. The optical power

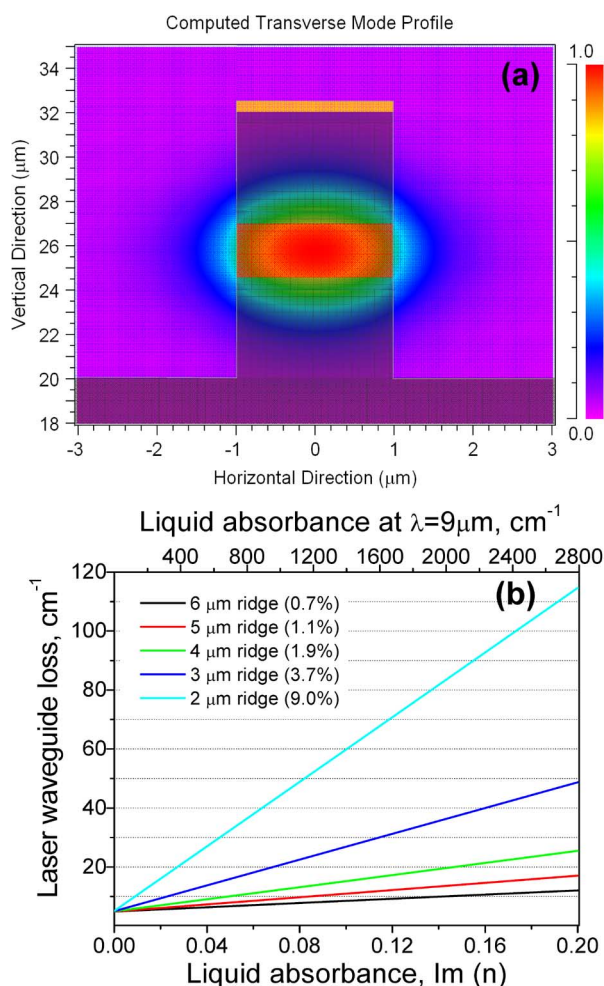


Fig. 24. (a) Simulated electric field distribution for a TM_{00} mode in a deep-etched 2- μm -wide ridge QCL with a gold electrical contact on top, surrounded by a liquid. (b) Dependence of the TM_{00} laser mode losses on liquid absorbance for deep-etched ridge waveguide QCLs with various ridge widths. Also listed is the percentage of modal overlap with the liquid (in intensity) for ridges of various widths. Liquid refractive index, $\text{Re}(n)$, is assumed to be 1.3 in the simulations. Simulations were performed using BeamPROP (R-Soft Design Group, Inc.) and COMSOL Multiphysics (COMSOL, Inc.).

of the applied laser available at the target wavelength was ~ 10 mW. At this operating condition and utilizing a liquid nitrogen cooled photodetector ($D^* = 10^{11} \text{ cm Hz}^{1/2} \text{ W}^{-1}$) the normalized sensitivity (1σ) of the sensor to NO concentration was $2.4 \text{ ppb Hz}^{-1/2}$, which allows a real time exhaled NO analysis (with single point averaging time of 1 sec) with a 2.4 ppbv precision. Application of a more powerful $\lambda = 5.26 \mu\text{m}$ ($\sim 1900 \text{ cm}^{-1}$) QC laser (e.g., 100 mW, which is a realistic assumption at this wavelength [77]) would allow to use a thermoelectrically cooled mid-IR detector (such detectors with a $D^* > 10^{10} \text{ cm Hz}^{1/2} \text{ W}^{-1}$ are commercially available) to improve NO sensor performance with a sub-ppbv precision. Such an improvement will lead to a truly portable, compact sensor suitable for *in situ* clinical studies.

D. Sensing of Fluids Using Quantum Cascade Lasers

Another promising area of QCL applications is mid-IR spectroscopic measurement of fluids, in particular for various microfluidic “lab-on-a-chip” systems. Microfluidics is a

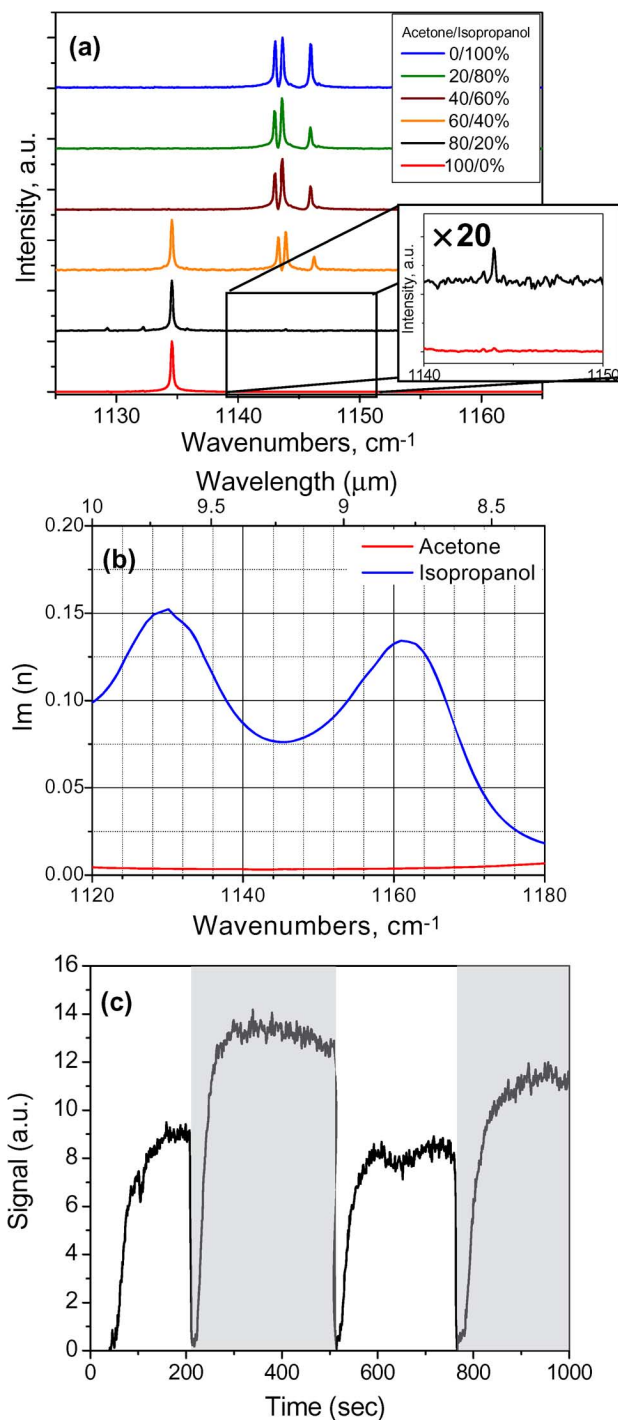


Fig. 25. (a) Emission spectra of an encapsulated device immersed in various mixtures of isopropanol and acetone. (b) Absorption spectra of isopropanol and acetone, represented as imaginary part of refractive index versus wavenumbers. (c) Emission power from an encapsulated device immersed in (a) acetone (shaded areas) and a 1% volume solution of isopropanol in acetone (clear areas).

growing field with important applications in biotechnology, chemical synthesis, and medicine [75]–[77], [81]. Microfluidic devices offer the ability to work with smaller reagent volumes, shorter reaction times, and the possibility of parallel operation. For a truly compact “lab-on-a-chip” system, one needs to have miniature elements for chemical analysis.

The small volume of analyte used in microfluidic systems often makes it difficult to use conventional absorption measurements for analysis because of the limited optical path length [81]. To address this problem, we have demonstrated a microfluidic QCL-based intra-cavity absorption spectroscopy (ICAS) sensor [83]. Laser ICAS has been long used as a highly sensitive spectroscopic technique [84]. In this method, the analyte is placed within the laser cavity and absorption lines of the analyte modify the laser losses, causing significant changes in the laser threshold and emission spectrum. QCLs can be designed with a very large homogeneously broadened gain bandwidth, with full-width at half-maximum (FWHM) of $\sim 300 \text{ cm}^{-1}$ [28], which is significantly larger than a typical FWHM of the absorption lines of liquids in mid-IR ($\sim 20 \text{ cm}^{-1}$) and makes sensitive microfluidic ICAS possible [6].

Our sensor is based a deep-etched narrow-ridge QCL with the ridge walls exposed to a liquid [83]. For a sufficiently small ridge width, the evanescent tails of the laser mode have significant overlap with the liquid on both sides of the ridge [Fig. 24(a)]. The liquid absorption lines modify the modal loss, as shown in Fig. 24(b), and cause a change in the QCL threshold current and emission spectrum. The evanescent tails of the laser mode are localized within $\sim 200 \text{ nm}$ of the ridge walls, and the required liquid volume for sensing is only ~ 10 picoliters, assuming a 2.5-mm-long, $10\text{-}\mu\text{m}$ -high laser ridge.

For an experimental demonstration of a microfluidic ICAS QCL sensor, we used a $5\text{-}\mu\text{m}$ -wide 2.5-mm-long ridge devices with back facet coating, processed from a BtC material and encapsulated into poly-dimethyl-siloxane (PDMS) chambers with a silicon window in front of the laser facet. For chemical detection, laser ICAS techniques utilize either laser emission spectrum changes or laser threshold changes due to analyte absorption [84]. We demonstrated both approaches with our QCL ICAS microfluidic sensors, using different mixtures of isopropanol and acetone. In Fig. 25(a), we show the emission spectra a device submerged in different mixtures of isopropanol and acetone. The spectra were taken at pump currents close to the peak of the laser light output, using 20-ns pulses at a repetition rate of 80 kHz. The absorption spectra of the liquids are shown in Fig. 25(b). The laser emission frequency clearly shifts from the peak of the laser gain position at approximately 1134 cm^{-1} to the minimum of isopropanol absorption position at $1143\text{--}1146 \text{ cm}^{-1}$ as the fraction of isopropanol in the solution rises.

In the other approach for chemical detection, we set the pump current slightly above threshold for a device on a temperature-stabilized heatsink and detect the laser peak output power change as the device becomes sequentially immersed in acetone and a 1% volume solution of isopropanol in acetone, Fig. 25(c). Here, we utilize the fact that the laser emission power near threshold is very sensitive to the amount of pump current in excess of the threshold value [84]. The laser power stabilizes shortly after the liquid is injected in PDMS chamber as the temperature of the liquid becomes that of the heat-sink. Because of isopropanol absorption, the threshold current for a device submerged in a 1% isopropanol solution in acetone is higher than that for a device submerged in acetone only, resulting in lower laser output power at a fixed current.

The sensitivity of ICAS is described using the effective absorption length, L_{eff} , defined as the cell path length required to obtain the equivalent signal change due to analyte absorption in traditional absorption spectroscopy [84],

$$L_{\text{eff}} = -\frac{\ln(I/I_0)}{\alpha} \quad (5)$$

where I_0 is the ICAS signal without analyte, I is the signal with analyte, and $\alpha = 4\pi \text{Im}(n)/\lambda$ is the absorbance of the analyte, n being the refractive index. For the data presented in Fig. 25(c), we estimate $I/I_0 \approx 0.75$ and obtain $L_{\text{eff}} \approx 170 \mu\text{m}$. We expect to improve L_{eff} in our sensors several fold in our future work, by utilizing devices with narrower ridges, improved processing, better temperature control, and a more stable power supply [83].

ACKNOWLEDGMENT

The authors acknowledge useful discussions and collaborations with O. Assayag, B. Lee, M. Loncar, D. Mars, A. Tandon, and J. Zhu.

REFERENCES

- [1] J. Faist, F. Capasso, D. L. Sivco, C. Sirtori, A. L. Hutchinson, and A. Y. Cho, "Quantum cascade laser," *Science*, vol. 264, pp. 553–556, 1994.
- [2] F. Capasso, R. Paiella, R. Martini, R. Colombelli, C. Gmachl, T. L. Myers, M. S. Taubman, R. M. Williams, C. G. Bethea, K. Unterrainer, H. Y. Hwang, D. L. Sivco, A. Y. Cho, A. M. Sergent, H. C. Liu, and E. A. Whittaker, "Quantum cascade lasers: Ultrahigh-speed operation, optical wireless communication, narrow linewidth, and far-infrared emission," *IEEE J. Quantum Electron.*, vol. 38, no. 6, pp. 511–514, Jun. 2002.
- [3] F. Capasso, C. Gmachl, D. L. Sivco, and A. Y. Cho, "Quantum cascade lasers," *Physics Today*, vol. 55, pp. 34–38, 2002.
- [4] C. Sirtori, H. Page, and C. Becker, "GaAs-based quantum cascade lasers," *Phil. Trans. Roy. Soc. Lond. A*, vol. 359, pp. 505–522, 2001.
- [5] J. Devenson, D. Barate, O. Cathabard, R. Teissier, and A. N. Baranov, "Very short wavelength ($\lambda = 3.1\text{--}3.3 \mu\text{m}$) quantum cascade lasers," *Appl. Phys. Lett.*, vol. 89, pp. 191115–191117, 2006.
- [6] G. Dehlinger, L. Diehl, U. Gennser, H. Sigg, J. Faist, K. Ennsin, D. Grutzmacher, and E. Muller, "Intersubband electroluminescence from silicon-based quantum cascade structures," *Science*, vol. 290, pp. 2277–2280, 2000.
- [7] R. P. Green, A. Krysa, J. S. Roberts, D. G. Revin, L. R. Wilson, E. A. Zibik, W. H. Ng, and J. W. Cockburn, "Room-temperature operation of InGaAs/AlInAs quantum cascade lasers grown by metalorganic vapor phase epitaxy," *Appl. Phys. Lett.*, vol. 83, pp. 1921–1923, 2003.
- [8] A. Evans, J. S. Yu, J. David, L. Doris, K. Mi, S. Slivken, and M. Razeghi, "High-temperature, high-power, continuous-wave operation of buried heterostructure quantum-cascade lasers," *Appl. Phys. Lett.*, vol. 84, pp. 314–316, 2004.
- [9] D. Bour, M. Troccoli, F. Capasso, S. Corzine, A. Tandon, D. Mars, and G. Hofler, "Metalorganic vapor phase epitaxy of room temperature, low threshold, InGaAs/AlInAs quantum cascade lasers," *J. Cryst. Growth*, vol. 272, pp. 526–530, 2004.
- [10] J. Faist, F. Capasso, D. Sivco, A. L. Hutchinson, S. N. G. Chu, and A. Y. Cho, "Short wavelength ($\lambda \sim 3.4 \mu\text{m}$) quantum cascade laser based on strained compensated InGaAs/AlInAs," *Appl. Phys. Lett.*, vol. 72, pp. 680–682, 1998.
- [11] R. Colombelli, F. Capasso, C. Gmachl, A. L. Hutchinson, D. L. Sivco, A. Tredicucci, M. C. Wanke, A. M. Sergent, and A. Y. Cho, "Far-infrared surface-plasmon quantum-cascade lasers at $21.5 \mu\text{m}$ and $24 \mu\text{m}$ wavelengths," *Appl. Phys. Lett.*, vol. 78, pp. 2620–2622, 2001.
- [12] J. S. Yu, S. Slivken, A. Evans, S. R. Darvish, J. Nguyen, and M. Razeghi, "High-power $\lambda \sim 9.5 \mu\text{m}$ quantum-cascade lasers operating above room temperature in continuous-wave mode," *Appl. Phys. Lett.*, vol. 88, pp. 091113–091115, 2006.
- [13] A. Gomez-Iglesias, D. Wassermann, C. Gmachl, A. Belyanin, and D. L. Sivco, "Electronic Anti-Stokes Raman emission in quantum cascade lasers," *Appl. Phys. Lett.*, vol. 87, pp. 261113–261115, 2005.

- [14] M. A. Belkin, F. Capasso, A. Belyanin, D. L. Sivco, A. Y. Cho, D. C. Oakley, C. J. Vineis, and G. W. Turner, "Terahertz quantum-cascade-laser source based on intracavity difference-frequency generation," *Nature Photon.*, vol. 1, pp. 288–292, 2007.
- [15] M. A. Belkin, M. Troccoli, D. Diehl, F. Capasso, A. A. Belyanin, D. L. Sivco, and A. Y. Cho, "Quasiphase matching of second-harmonic generation in quantum cascade lasers by Stark shift of electronic resonances," *Appl. Phys. Lett.*, vol. 88, pp. 201108–201110, 2006.
- [16] R. Colombelli, K. Srinivasan, M. Troccoli, O. Painter, C. Gmachl, D. M. Tennant, A. M. Sergent, D. L. Sivco, A. Y. Cho, and F. Capasso, "Quantum cascade surface-emitting photonic crystal laser," *Science*, vol. 302, pp. 1374–1377, 2003.
- [17] R. Kohler, A. Tredicucci, F. Beltram, H. Beere, E. Linfield, A. Giles Davies, D. Ritchie, R. Iotti, and F. Rossi, "Terahertz semiconductor heterostructure laser," *Nature*, vol. 417, pp. 156–159, 2002.
- [18] A. Lops, V. Spagnolo, and G. Scarmacio, "Thermal modeling of GaInAs/AlInAs quantum cascade lasers," *J. Appl. Phys.*, vol. 100, pp. 43109–43113, 2006.
- [19] M. Beck, D. Hofstetter, T. Aellen, J. Faist, U. Oesterle, M. Ilegems, E. Gini, and H. Melchior, "Continuous wave operation of a mid-infrared semiconductor laser at room temperature," *Science*, vol. 295, pp. 301–305, 2002.
- [20] M. Troccoli, D. Bour, S. Corzine, G. Hoeffler, A. Tandon, D. Mars, L. Diehl, and F. Capasso, "High-temperature, high power, continuous wave operation of quantum cascade lasers grown by metalorganic vapor phase epitaxy," *Appl. Phys. Lett.*, vol. 85, pp. 5842–5844, 2004.
- [21] M. Troccoli, S. Corzine, D. Bour, J. Zhu, O. Assayag, L. Diehl, B. G. Lee, G. Hoeffler, and F. Capasso, "Room temperature continuous wave operation of quantum cascade lasers grown by metalorganic vapor phase epitaxy," *Electron. Lett.*, vol. 41, pp. 1059–1061, 2005.
- [22] L. Diehl, D. Bour, S. Corzine, J. Zhu, G. Höfler, M. Loncar, M. Troccoli, and F. Capasso, "High-temperature continuous wave operation of strain-balanced quantum cascade lasers grown by metal organic vapor-phase epitaxy," *Appl. Phys. Lett.*, vol. 89, pp. 081101–081103, 2006.
- [23] L. Diehl, D. Bour, S. Corzine, J. Zhu, G. Höfler, M. Loncar, M. Troccoli, and F. Capasso, "High-power quantum cascade lasers grown by low-pressure metal organic vapor-phase epitaxy operating in continuous wave above 400 K," *Appl. Phys. Lett.*, vol. 88, pp. 201115–201117, 2006.
- [24] L. Diehl, D. Bour, S. Corzine, J. Zhu, G. Höfler, B. G. Lee, C. Y. Wang, M. Troccoli, and F. Capasso, "Pulsed- and continuous-mode operation at high temperature of strained quantum-cascade lasers grown by metalorganic vapor phase epitaxy," *Appl. Phys. Lett.*, vol. 88, pp. 41102–41104, 2006.
- [25] C. Gmachl, A. Tredicucci, F. Capasso, A. L. Hutchinson, D. L. Sivco, J. N. Baillargeon, and A. Y. Cho, "High-power $\lambda = 8$ mm quantum cascade lasers with near optimum performance," *Appl. Phys. Lett.*, vol. 72, pp. 3130–3133, 1998.
- [26] S. Blaser, D. Yarekha, L. Hvozdar, Y. Bonetti, A. Muller, M. Giovannini, and J. Faist, "Room-temperature, continuous-wave, single-mode quantum-cascade lasers at $\lambda \sim 5.4$ μm ," *Appl. Phys. Lett.*, vol. 86, pp. 41109–41111, 2005.
- [27] C. Sirtori, F. Capasso, J. Faist, A. L. Hutchinson, D. L. Sivco, and A. Y. Cho, "Resonant tunneling in quantum cascade lasers," *IEEE J. Quantum Electron.*, vol. 34, pp. 1722–1729, 1998.
- [28] J. Faist, M. Beck, T. Aellen, and E. Gini, "Quantum cascade lasers based on a bound-to-continuum transition," *Appl. Phys. Lett.*, vol. 78, pp. 147–149, 2001.
- [29] L. A. Coldren and S. W. Corzine, *Diode Lasers and Photonics Integrated Circuits*. New York: Wiley, 1995.
- [30] C. Gmachl, F. Capasso, D. L. Sivco, and A. Y. Cho, "Recent progress in quantum cascade lasers and applications," *Rep. Prog. Phys.*, vol. 64, pp. 1533–1601, 2001.
- [31] C. Sirtori, J. Faist, F. Capasso, D. L. Sivco, A. L. Hutchinson, and A. Y. Cho, "Quantum cascade laser with plasmon-enhanced waveguide operating at 8.4 μm wavelength," *Appl. Phys. Lett.*, vol. 66, pp. 3242–3244, 1995.
- [32] J. Faist, F. Capasso, C. Sirtori, D. L. Sivco, and A. Y. Cho, "Quantum cascade lasers," in *Intersubband Transitions in Quantum Wells*, H. C. Liu and F. Capasso, Eds. New York: Academic Press, 2000, vol. 66, Semiconductors and Semimetals, For a discussion on the estimate of J at threshold see.
- [33] C. Gmachl, D. L. Sivco, R. Colombelli, F. Capasso, and A. Y. Cho, "Ultra-broadband semiconductor laser," *Nature*, vol. 415, pp. 883–887, 2002.
- [34] R. Maulini, A. Mohan, M. Giovannini, J. Faist, and E. Gini, "External cavity quantum-cascade lasers tunable from 8.2 to 10.4 μm using a gain element with a heterogeneous cascade," *Appl. Phys. Lett.*, vol. 88, pp. 201113–201113, 2006.
- [35] F. Zenhausern, M. P. O'Boyle, and H. K. Wickramasinghe, "Apertureless near-field optical microscope," *Appl. Phys. Lett.*, vol. 65, pp. 1623–1625, 1994.
- [36] A. Lahrech, R. Bachelot, P. Gleyzes, and A. C. Boccard, "Infrared-reflection-mode near-field microscopy using an apertureless probe with a resolution of $\lambda/600$," *Opt. Lett.*, vol. 21, pp. 1315–1318, 1996.
- [37] V. Moreau, M. Barhiz, R. Colombelli, P. A. Lemoine, Y. De Wilde, L. R. Wilson, and A. B. Krysa, "Direct imaging of a laser mode via midinfrared near-field microscopy," *Appl. Phys. Lett.*, vol. 90, pp. 201114–201116, 2007.
- [38] B. Knoll and F. Keilmann, "Enhanced dielectric contrast in scattering-type scanning near-field optical microscopy," *Opt. Commun.*, vol. 182, pp. 321–328, 2000.
- [39] M. F. C. Schemmann, C. J. van der Poel, B. A. H. van Bakel, H. P. M. M. Ambrosius, A. Valster, J. A. M. van den Heijkant, and G. A. Acket, "Kink power in weakly index guided semiconductor lasers," *Appl. Phys. Lett.*, vol. 66, pp. 920–922, 1995.
- [40] W. W. Bewley, J. R. Lindle, C. S. Kim, I. Vurgaftman, J. R. Meyer, A. J. Evans, J. S. Yu, S. Slivken, and M. Razeghi, "Beam steering in high-power CW quantum-cascade lasers," *IEEE J. Quantum Electron.*, vol. 41, no. 6, pp. 833–841, Jun. 2005.
- [41] N. Yu *et al.*, manuscript in preparation.
- [42] J. Faist, D. Hofstetter, M. Beck, T. Aellen, M. Rochat, and S. Blaser, "Bound-to-continuum and two-phonon resonance quantum cascade lasers for high duty cycle, high temperature operation," *IEEE J. Quantum Electron.*, vol. 38, no. 6, pp. 533–546, Jun. 2002.
- [43] V. Spagnolo, G. Scarmacio, H. Page, and C. Sirtori, "Simultaneous measurement of the electronic and lattice temperatures in GaAs/Al_{0.55}Ga_{0.45} quantum-cascade lasers: Influence on the optical performance," *Appl. Phys. Lett.*, vol. 84, pp. 3690–3692, 2004.
- [44] R. Paiella, F. Capasso, C. Gmachl, D. L. Sivco, J. N. Baillargeon, A. L. Hutchinson, A. Y. Cho, and H. C. Liu, "Self-mode-locking of quantum cascade lasers with giant ultrafast optical nonlinearities," *Science*, vol. 290, pp. 1739–1742, 2000.
- [45] C. Y. Wang, L. Diehl, A. Gordon, C. Jirauschek, F. X. Kartner, A. Belyanin, D. Bour, S. Corzine, G. Höfler, M. Troccoli, J. Faist, and F. Capasso, "Coherent instabilities in a semiconductor laser with fast gain recovery," *Phys. Rev. A*, vol. 75, p. 031802(R), 2007.
- [46] A. Gordon *et al.*, unpublished.
- [47] H. Risken and K. Nummedal, "Self-pulsing in lasers," *J. Appl. Phys.*, vol. 39, pp. 4662–4672, 1968.
- [48] P. Graham and H. Haken, *Z. Phys.*, vol. 213, p. 420, 1968.
- [49] F. K. Tittel, D. Richter, and A. Fried, "Mid-infrared laser applications in spectroscopy," in *Solid State Mid-Infrared Laser Sources*, I. T. Sorokina and K. L. Vodopyanov, Eds. New York: Springer Verlag, 2003, vol. 89, Topics in Appl. Phys., pp. 445–510.
- [50] R. F. Curl and F. K. Tittel, "Tunable infrared laser spectroscopy," *Annu. Rep. Prog. Chemistry*, vol. 98, pp. 219–272, 2002, sec. C.
- [51] T. Yanagawa, H. Kanbara, O. Tadanaga, M. Asobe, H. Suzuki, and J. Yumoto, "Broadband difference frequency generation around phase-match singularity," *Appl. Phys. Lett.*, vol. 86, p. 161106, 2005.
- [52] D. Richter and P. Weibring, "Ultra high precision mid-IR spectrometer: Design and analysis of an optical fiber pumped difference frequency generation source," *Appl. Phys. B*, vol. 82, pp. 479–486, 2006.
- [53] A. A. Kosterev and F. K. Tittel, "Chemical sensors based on quantum cascade lasers," *IEEE J. Quantum Electron.*, vol. 38, Special Issue on QC Lasers, no. 6, pp. 582–591, Jun. 2002.
- [54] R. Maulini, M. Beck, J. Faist, and E. Gini, "2004: Broadband tuning of external cavity bound-to-continuum quantum-cascade lasers," *Appl. Phys. Lett.*, vol. 84, p. 1659, 2004.
- [55] G. Wysocki, R. F. Curl, F. K. Tittel, R. Maulini, J. M. Bulliard, and J. Faist, "Widely tunable mode-hop free external cavity quantum cascade laser for high resolution spectroscopic applications," *Appl. Phys. B*, vol. 81, pp. 769–777, 2005.
- [56] C. Peng, G. Luo, and H. Q. Le, "Broadband, continuous, and fine-tune properties of external-cavity thermoelectric-stabilized mid-infrared quantum-cascade lasers," *Appl. Opt.*, vol. 42, pp. 4877–4882, 2003.
- [57] G. C. Liang, H.-H. Liu, A. H. Kung, A. Mohacs, A. Miklos, and P. Hess, "Photoacoustic trace detection of methane using compact solid-state lasers," *J. Phys. Chem. A*, vol. 104, pp. 10179–10183, 2000.

- [58] M. Gomes Da Silva, A. Miklos, A. Falkenroth, and P. Hess, "Photoacoustic measurement of N₂O concentrations in ambient air with a pulsed optical parametric oscillator," *Appl. Phys. B*, vol. 82, pp. 329–336, 2006.
- [59] A. A. Kosterev, Y. A. Bakhrin, R. F. Curl, and F. K. Tittel, "Quartz-enhanced photoacoustic spectroscopy," *Opt. Lett.*, vol. 27, pp. 1902–1904, 2002.
- [60] A. A. Kosterev, F. K. Tittel, D. Serebryakov, A. Malinovsky, and A. Morozov, "Applications of quartz tuning fork in spectroscopic gas sensing," *Rev. Scientif. Instrum.*, vol. 76, p. 043105, 2005.
- [61] A. A. Kosterev and F. K. Tittel, "Ammonia detection by use of quartz-enhanced photoacoustic spectroscopy with a near-IR telecommunication diode laser," *Appl. Opt.*, vol. 43, pp. 6213–6217, 2004.
- [62] G. Wysocki, A. A. Kosterev, and F. K. Tittel, "Influence of molecular relaxation dynamics on quartz-enhanced photoacoustic detection of CO₂ at $\lambda = 2 \mu\text{m}$," *Appl. Phys. B*, vol. 85, pp. 301–306, 2006.
- [63] D. Weidmann, A. A. Kosterev, F. K. Tittel, N. Ryan, and D. McDonald, "2004: Application of widely electrically tunable diode laser to chemical gas sensing with quartz-enhanced photoacoustic spectroscopy," *Opt. Lett.*, vol. 29, pp. 1837–1839, 2004.
- [64] A. A. Kosterev, Y. A. Bakhrin, and F. K. Tittel, "Ultrasensitive gas detection by quartz-enhanced photoacoustic spectroscopy in the fundamental molecular absorption bands region," *Appl. Phys. B*, vol. 80, pp. 133–138, 2005.
- [65] A. A. Kosterev, T. S. Mosely, and F. K. Tittel, "Impact of humidity on quartz enhanced photoacoustic spectroscopy based detection of HCN," *Appl. Phys. B*, vol. 85, pp. 295–300, 2006.
- [66] A. A. Kosterev, Y. A. Bakhrin, F. K. Tittel, S. Blaser, Y. Bonetti, and L. Hvozdar, "Photoacoustic phase shift as a chemically selective spectroscopic parameter," *Appl. Phys. B (Rapid Communications)*, vol. 78, pp. 673–676, 2004.
- [67] M. Horstjann, Y. A. Bakhrin, A. A. Kosterev, R. F. Curl, and F. K. Tittel, "Formaldehyde sensor using interband cascade laser based quartz-enhanced photoacoustic spectroscopy," *Appl. Phys. B*, vol. 79, pp. 799–803, 2004.
- [68] A. Kosterev, F. K. Tittel, T. S. Knittel, A. Cowie, and J. D. Tate, "Trace humidity sensor based on quartz-enhanced photoacoustic spectroscopy," in *Laser Application to Chemical Security and Environmental Analysis Conference*, Incline Village, NV, Feb. 5–9, 2006.
- [69] M. D. Wojcik, M. C. Phillips, B. D. Cannon, and M. S. Taubman, "Gas phase photoacoustic sensor at 8.41 μm using quartz tuning forks and amplitude modulated quantum cascade lasers," *Appl. Phys. B*, vol. 85, pp. 307–313, 2006.
- [70] G. Wysocki, A. A. Kosterev, and F. K. Tittel, "Spectroscopic trace-gas sensor with rapidly scanned wavelengths of a pulsed quantum cascade laser for in situ NO monitoring of industrial exhaust systems," *Appl. Phys. B*, vol. 80, pp. 617–625, 2005.
- [71] A. A. Kosterev, A. L. Malinovsky, F. K. Tittel, C. Gmachl, F. Capasso, D. L. Sivco, J. N. Baillargeon, A. L. Hutchinson, and A. Y. Cho, "Cavity ring-down spectroscopy of NO with a single frequency quantum cascade laser," *Appl. Opt.*, vol. 40, pp. 5522–5529, 2001.
- [72] G. Berden, R. Peeters, and G. Meijer, "Cavity ring-down spectroscopy, Experimental schemes and applications," *Int. Rev. Phys. Chem.*, vol. 19, pp. 565–607, 2000.
- [73] Y. A. Bakhrin, A. A. Kosterev, C. Roller, R. F. Curl, and F. K. Tittel, "Mid-infrared quantum cascade laser based off-axis integrated cavity output spectroscopy for biogenic NO detection," *Appl. Opt.*, vol. 43, pp. 2257–2266, 2004.
- [74] M. L. Silva, D. M. Sonnenfroh, D. I. Rosen, M. G. Allen, and A. O'Keefe, "Integrated cavity output spectroscopy measurements of nitric oxide levels in breath with a pulsed room-temperature quantum cascade laser," *Appl. Phys. B*, vol. 81, pp. 705–710, 2005.
- [75] M. McCurdy, Y. A. Bakhrin, and F. K. Tittel, "Quantum cascade laser-based integrated cavity output spectroscopy of exhaled nitric oxide," *Appl. Phys. B*, vol. 85, pp. 445–452, 2006.
- [76] K. Namjou, C. B. Roller, T. E. Reichl, J. D. Jeffers, G. L. McMillen, P. J. McCann, and M. A. Camp, "Determination of exhaled nitric oxide distributions in a diverse sample population using tunable diode laser absorption spectroscopy," *Appl. Phys. B*, vol. 85, pp. 427–435, 2006.
- [77] J. B. McManus, D. D. Nelson, S. C. Herndon, J. H. Shorter, M. S. Zahniser, S. Blaser, L. Hvozdar, A. Muller, M. Giovannini, and J. Faist, "Comparison of cw and pulsed operation with a TE-cooled quantum cascade infrared laser for detection of nitric oxide at 1900 cm⁻¹," *Appl. Phys. B*, vol. 85, pp. 235–241, 2006.
- [78] D. Erickson and D. Li, "Integrated microfluidic devices," *Anal. Chim. Acta*, vol. 507, pp. 11–26, 2004.
- [79] D. Psaltis, S. R. Quake, and C. Yang, "Developing optofluidic technology through the fusion of microfluidics and optics," *Nature*, vol. 442, pp. 381–386, 2006.
- [80] C. Monat, P. Domachuk, and B. J. Eggleton, "Integrated optofluidics: A new river of light," *Nature Photon.*, vol. 1, pp. 106–114, 2007.
- [81] E. Verpoorte, "Chip vision—Optics for microchips," *Lab Chip*, vol. 3, pp. 42N–52N, 2003.
- [82] B. G. Lee, R. Audet, J. MacArthur, M. A. Belkin, L. Diehl, C. Pflugl, F. Capasso, D. C. Oakley, D. Chapman, A. Napoleone, G. Turner, D. Bour, S. Corzine, and G. Höfler, "Widely tunable single mode quantum cascade laser source for mid-infrared spectroscopy," *Appl. Phys. Lett.*, submitted for publication.
- [83] M. A. Belkin, M. Lončar, B. G. Lee, C. Pflugl, R. Audet, L. Diehl, F. Capasso, D. Bour, S. Corzine, J. Zhu, and G. Höfler, "Intra-cavity absorption spectroscopy with narrow-ridge microfluidic quantum cascade lasers," *Opt. Express*, accepted for publication.
- [84] V. M. Baev, T. Latz, and P. E. Toschek, "Laser intracavity absorption spectroscopy," *Appl. Phys. B*, vol. 69, pp. 171–202, 1999.

Mariano Troccoli (M'02) was born in Bari, Italy, in 1974. He received the Ph.D. degree in quantum electronics from the Polytechnic of Bari in 2001 and the M.S. degree in theoretical physics (*magna cum laude*) from the University of Bari in 1997.

He is a co-Founder and Director of device research at Argos Tech, LLC, a start-up company in Santa Clara, CA. Previously, he was a Research Associate Fellow at Harvard University, Cambridge, MA, and a Postdoctoral Member of Technical Staff at Bell Labs, Murray Hill, NJ. He co-authored more than 35 journal articles and book chapters and more than five patents. He is currently working on high-performance quantum cascade lasers and sensors.

Dr. Troccoli is a member of APS, OSA, and was invited to *Who's Who in America* since 2007. He was awarded the "Young Investigator Award" of the European Material Research Society in 2001.

Laurent Diehl was born in Switzerland in 1976. He received the Ph.D. degree from the University of Neuchâtel, Neuchâtel, Switzerland, in 2003. His work concentrated on the development of p-type Si/SiGe quantum cascade lasers.

He joined the group of Prof. F. Capasso at Harvard University, Cambridge, in 2003 as a Postdoctoral Fellow and later as a Research Associate. His work currently focuses on the development of high-power quantum-cascade lasers grown by MOCVD, as well as the physics of these devices, including their ultrafast dynamics.

Dr. Diehl was the co-recipient of the Swiss Physical Society's IBM award in 2001.

David P. Bour, photograph and biography not available at the time of publication.

Scott W. Corzine was born in Nashville, TN, in 1963. He received the B.S., M.S., and Ph.D. degrees from the Department of Electrical and Computer Engineering, University of California at Santa Barbara. His graduate work involved the theoretical and experimental investigation of vertical-cavity surface-emitting lasers.

He has co-authored a graduate-level textbook on semiconductor lasers and has also contributed a chapter to a book on quantum well lasers. He was with Agilent Laboratories, Palo Alto, CA, for ten years, working on the design and fabrication of various optoelectronic devices. He is currently with Infinera, Sunnyvale, CA.

Nanfeng Yu received the B.S. degree in electronic information science and technology from the Department of Electronics, Peking University, Beijing, China, in 2004. He is currently working toward the Ph.D degree in the School of Engineering and Applied Sciences, Harvard University, Cambridge, MA. His research interests include near-field microscopy, mid-infrared plasmonics (e.g., mid-infrared antennas), and the physics of quantum-cascade lasers (e.g. lateral mode locking).

Christine Y. Wang was born in Taipei, Taiwan, in 1980. She received the B.S. degree in physics from National Taiwan University, Taipei, Taiwan, R.O.C., in 2002 and the M.S. degree in physics in 2004 from Harvard University, Cambridge, MA, where she is currently working toward the Ph.D. degree.

She joined the group of Prof. Capasso in August, 2004, where she is working on the instability/mode-locking phenomena in quantum cascade lasers.

Mikhail A. Belkin was born in Syzran, Russia, in 1977. He received the B.S. degree in physics and mathematics from Moscow Institute of Physics and Technology, Moscow, Russia, in 1998 and the Ph.D. degree in physics from the University of California at Berkeley in 2004. His Ph.D. work was focused on the development of novel nonlinear spectroscopic methods.

He is presently a Research Associate with the Harvard School of Engineering and Applied Sciences, Harvard University, Cambridge, MA. His research interests include, among others, the development of terahertz quantum cascade lasers, nonlinear optical effects in quantum cascade lasers, and the development of widely tunable compact mid-infrared sources for spectroscopic applications.

Gloria Höfler, photograph and biography not available at the time of publication.

Rafal Lewicki was born in Gubin, Poland, in 1980. He received the Master's degree in 2005 from Wrocław University of Technology, Wrocław, Poland, where he is currently working toward the Ph.D. degree.

In December 2005, as a visiting student, he joined the Laser Science Group at Rice University, Houston TX. His research interests concern laser spectroscopic trace gas detection techniques. His current activities focus on development of widely tunable sensor platform enabling broadband and high-resolution spectroscopic measurements.

Gerard Wysocki was born in Jelenia Gora, Poland, in 1974. He received the Master's degree in electronic from the Wrocław University of Technology, Wrocław, Poland, in 1999 and the Ph.D. degree in physics in 2003 from Johannes Kepler University, Linz, Austria. His Ph.D. research was focused on the application of near-field optics in laser induced chemical processing.

In August 2003, he joined the Laser Science Group of Prof. Frank Tittel in the Department of Electrical and Computer Engineering, Rice University, Houston, TX. His current research interests are focused on various molecular absorption spectroscopy techniques used for detection of trace gases in environmental, industrial, medical, and fundamental science applications, as well as the development of new tunable laser sources suitable for performing of high-resolution molecular spectroscopy.

Frank K. Tittel (SM'72–F'86) was born in Berlin, Germany, in 1933. He received the Bachelor's, Master's, and Doctorate degrees in physics from the University of Oxford, Oxford, U.K., in 1955 and 1959, respectively. He also received a Dr. Sci. (HC) degree from JATE University, Szeged, Hungary, in 1993.

From 1959 to 1967, he was a Research Physicist with General Electric (G.E.) Research and Development Center, Schenectady, NY. At G.E., he carried out

early pioneering studies of dye lasers and high-power solid-state lasers. Since 1967, he has been on the Faculty of the Department of Electrical and Computer Engineering, Rice University, Houston, TX, where is currently an Endowed Chair Professor. In 1973 and 1981, he was an Alexander von Humboldt Senior Fellow at the Max-Planck Institutes of Biophysical Chemistry, Göttingen, Germany, and Quantum Optics, Munich, Germany, respectively. He held Visiting Professor appointments at NASA Goddard Space Flight Center, University of Aix-Marseille, Keio University (Japan), and the Swiss Institute of Technology (ETH-Zurich). His current research interests include various aspects of quantum electronics, in particular laser spectroscopy, nonlinear optics, and laser applications in environmental monitoring, process control, and medicine. He has published more than 300 technical papers and holds eight U.S. patents in these areas.

Prof. Tittel is a Fellow of the Optical Society of America and the American Physical Society. He is an Associate Editor of Applied Physics B, and a former Editor-in-Chief of IEEE JOURNAL OF SELECTED TOPICS IN QUANTUM ELECTRONICS (1996–1998) and Associate Editor of the IEEE JOURNAL OF QUANTUM ELECTRONICS. He has served on numerous technical program committees such as CLEO, IQEC, and QELS for OSA and APS.

Federico Capasso received the Dr. Phys. degree (*summa cum laude*) from the University of Rome, Rome, Italy, in 1973.

He is the Robert Wallace of Applied Physics and Vinton Hayes Senior Research Fellow in Electrical Engineering at Harvard University, Cambridge, MA. He then joined Fondazione Ugo Bordoni as a Researcher from 1974 to 1976. At the end of 1976, he joined Bell Laboratories, first as a Postdoctorate and then as a Member of Technical Staff until 1986, when he became head of the newly formed Quantum Phenomena and Device Research Department. In 1997, he became head of Semiconductor Physics Research and was made a Bell Labs Fellow for his scientific contributions. From 2000 to the end 2002, he was Vice President for Physical Research at Bell Laboratories, Lucent Technologies.

He is internationally known for his basic and applied research on the quantum design of new artificial materials and devices, known as band-structure engineering, which have opened up new directions in electronics, photonics, mesoscopic physics and nanotechnology and for his investigations of the Casimir effect and in surface plasmon nanophotonics, including his recent work on plasmonic laser antennas. Among his inventions is the quantum cascade laser, a fundamentally new light source, which has now been commercialized. Other He has co-authored over 300 papers, edited four volumes, and holds over 60 U.S. patents.

Dr. Capasso is a member of the National Academy of Sciences, the National Academy of Engineering, the American Academy of Arts and Sciences, and the European Academy of Science. His awards include the King Faisal International Prize for Science, the IEEE Edison Medal, the American Physical Society, the Arthur Schawlow Prize in Laser Science, the Wetherill Medal of the Franklin Institute, the Wood prize of the Optical Society of America (OSA), the William Streifer Award of the Laser and Electro-optic Society (IEEE), the Rank Prize in Optoelectronics (U.K.), the IEEE David Sarnoff Award in Electronics, the Duddell Medal of the Institute of Physics (U.K.), the Willis Lamb Medal for Laser Science and Quantum Optics, the Materials Research Society Medal, the "Vinci of Excellence" Prize (France), the Welker Memorial Medal (Germany), the New York Academy of Sciences Award, and the Newcomb Cleveland Prize of the American Association for the Advancement of Science. He is a Fellow of the Optical Society of America, the American Physical Society, the International Society for Optical Engineering (SPIE), and the American Association for the Advancement of Science (AAAS).